AirCargoChallenge 2022

Technical Report

Team #06

Olissipo Air Team

OLISSIPO AIR TEAM

INSTITUTO SUPERIOR TÉCNICO | ULISBOA

AIR CARGO CHALLENGE 2022

Olissipo Air Team - Team 06
Technical Report

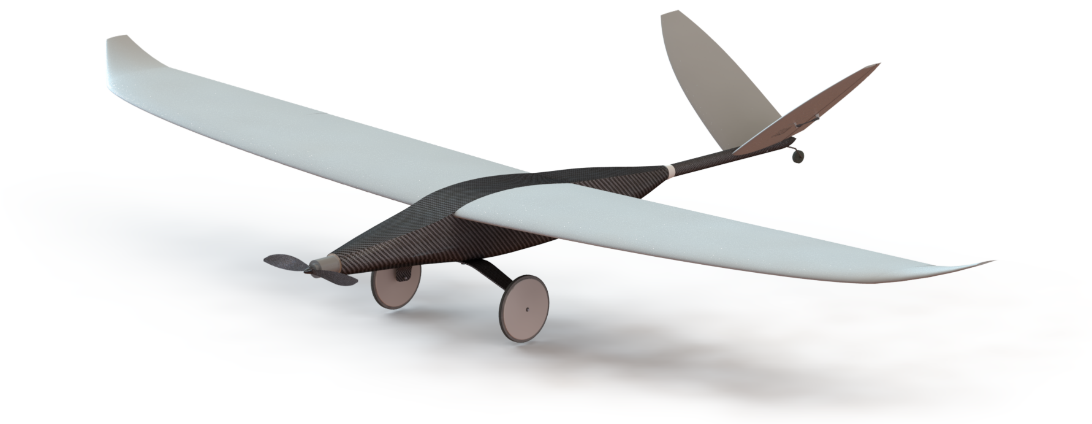

May 1, 2022

Table of Contents

List of Figures

List of Tables

1 Introduction

Olissipo Air Team stands as this competition's representative of Instituto Superior Técnico (IST), as well as that of AeroTéc - the Association of Aerospace Engineering Students of the aforementioned institution.

The aim of our student association is to provide students with the opportunity of complementing theoretical knowledge acquired in the classes with some much-needed practical experience in the aerospace engineering branch. Our team in particular offers the possibility of doing some hands-on work in designing, building and testing an aircraft.

None of the current team members have participated in this competition in the past, but have learned valuable lessons from older colleagues who, in 2020/21, laid the groundwork for the prototype upon which the current aircraft is based.

1.1 Team

In order to more efficiently design and build the aircraft, the team decided to partition itself into smaller groups that would be in charge of different components of the aircraft.

For structural design and construction, 3 subteams were assigned - one for the wing structure, one for the fuselage and one for the tail and landing gear. The aerodynamic design of the aircraft, on the other hand, particularly the shape of the wing and tail, are under the aerodynamics subteam's responsibility. There was also a need for an electronics subteam in charge of all the aircraft's electronic components. Finally, a marketing team was also assembled to optimize contacts with potential sponsors and the project's outreach program. The coordinators responsible for these task-forces, as well as the assistant professor and the pilot, are presented in Table 1.1. The full team can be found in **Annex B**.

In order to ensure all members are aware of the work other subteams are developing, general meetings are held every week, where the progress of each one is laid out. Furthermore, the subteams' coordinators arrange meetings of their own when they see fit, in order to, among other aspects, ensure a more cohesive workflow. This method has proven paramount in the progress made over the last 2 years.

Table 1.1: Coordination Team for Olissipo Air Team

Name	**Team position**	**Course (year)**
Simão Martins	Team Leader / Wing structures Coordinator	Aerospace Eng. (3^{rd})
Duarte Brito	Financial Coordinator / Aerodynamics Coordinator	Aerospace Eng. (3^{rd})
José Bento	Human Resources Coordinator / Electronics Coordinator	Aerospace Eng. (3^{rd})
Filipe Faria	Tail and Landing Gear Coordinator	Aerospace Eng. (5^{th})
Francisco Dores	Fuselage Coordinator	Aerospace Eng. (3^{rd})
Mariana Dias	Marketing Coordinator	Mechanical Eng. (5^{th})
Ludovico Lourenço	Pilot	-
André Marta	Supervising Professor	-

2 Project Management

2.1 Time Schedule

The time schedule for this academic year is shown in the Gant-Chart in Figure 2.1. Even though the time schedule only shows the tasks for this academic year, the work for Air Cargo Challenge 2022 started in 2020/21, when the regulations came out. The discussions on conceptual design of the UAV started on the beginning of the academic year of 2020/21 and, by the end of it, the first optimized prototype had already been designed and built.

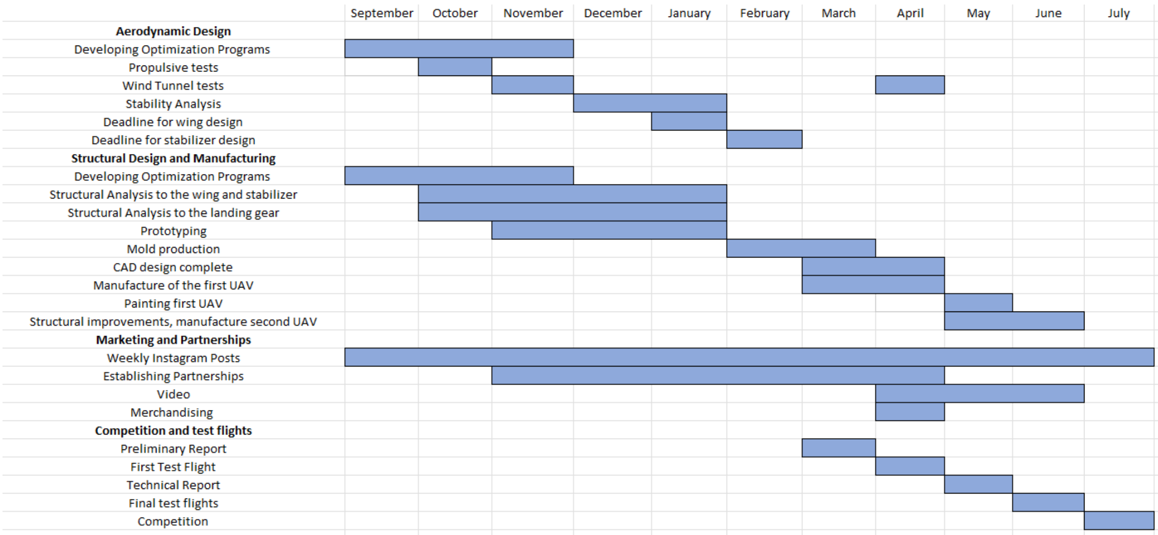

Figure 2.1: Time schedule for the academic year of 2021/22

During this academic year, the optimization tools were further developed, and a second iteration on the UAV design was made, based on the test flights and wind tunnel tests. This year, the team has conditions to finish building the UAV a few months ahead of the competition, to leave time for flight tests, to understand the limitations of our design and also to train the pilot. Furthermore, this would allow further structural improvements to the UAV after the initial tests and the manufacturing of spare parts for the competition.

Parallel to the design and manufacturing of the UAV, there were two recruitment seasons during the academic year, plus several new partnerships, as will be explored next.

2.2 Finances

Along with the team's growth, finances became an ever-increasing limiting factor. Even with help from the university, it was clear that the project could not support the entirety of the team's travelling costs. For the first time, the project did not cover the totality of the competition's expenditures (as seen in Figure 2.2). The airplane tickets required all the planned budget, but the limitation in guests limited the amount spent. As for the materials

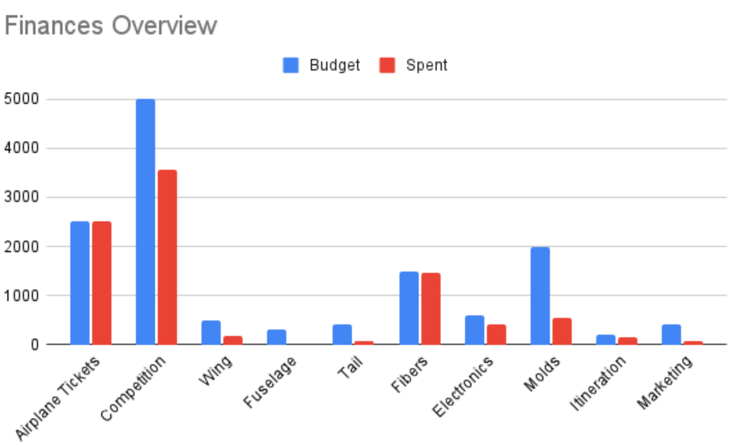

Figure 2.2: Project finances overview

needed for the airplane, the main differences appeared with sponsorships, as seen in Table 2.3. The main expenses predicted for the fuselage were regarding the specialized cores, which were provided by our sponsor, Lantor Composites. Blocks and Fablab also helped with 3D printing supplies. The decision to use wood instead of Sika for the wing and fuselage molds had a great impact as well. Note that some teams, such as the marketing team, have increased spending leading up to the competition, so this still haven't met their initial budget.

None of that would be possible without sponsor help, both monetary and logistical, from the following sponsors, to whom the team owes a great deal of gratitude. We note that Orion Technik, QSR and IST have been supporting the team for many iterations of the competition, to whom it is due a special thank-you message.

Figure 2.3: Project's sponsors information

Entity	Type of support	Amount / Material
ULisboa	Logistical	workshop space, exposure, etc.
IST	Logistical	workshop space, exposure, etc.
IPDJ	Financial	€949,71
IST & Santander Totta	Financial	€5000
Orion Technik	Financial	Material refunds
IST & Caixa Geral de Depósitos	Financial	€1450
QSR	Financial	€750
AED Cluster	Financial	€500 + AED days + exposure
EVOLEO Technologies	Financial	€500
Alma Design	Financial	€200 and aircraft styling
OMNI Aviation Group	Financial	€100
Rebelco	Financial	30% Discount
R&G Composites	Financial	20% Discount
Fablab	Logistical	3D printing services
Lantor Composites	Logistical	Core material
Força Aérea Portuguesa	Logistical	Wind tunnel
Blocks	Logistical	3D printer and 5kg of filament
Copitec	Logistical	€150 in marketing material

2.3 Tools Used

- Ansys Workbench (version 2019R1, 2020R1 and 2022R1);
- SolidWorks (versions 2020 and 2021);
- Ultimaker Cura (version 4.9.1);
- Matlab (versions 2020a and 2021a);
- Abaqus (version 2021);
- XFLR5 (version 6.48);
- Xfoil (version 6.48);
- HSMWorks (version 2021).

3 Aerodynamic Design

3.1 Propulsion

Before starting the aerodynamic design of the aircraft, it was necessary to establish how much thrust the engine could output. The regulation establishes the motor to use as the 'AXI 2826/10 GOLD LINE V2', as well as a 3 cell limit on the main battery. Therefore, the liberty to optimize the motor performance was limited to the battery capacity, discharge rate, a few ESC parameters and the choice between 2 different propellers.

3.1.1 ESC *Timing*

Regarding market researches, the 'Hobbywing Skywalker 40A ESC' was considered the ideal choice to plug to the required motor since it is neither too heavy nor too expensive.

The ESC's *Timing* affects the synchronization between the angular position of the magnet and the activation of the peripheral coils. This makes programming this parameter the best way to achieve the desired performance regarding the ESC. The completion of some tests showed that the thrust increases with the timing (for programmable values). Therefore, the ESC was programmed to its maximum *Timing* available (26.25°), as seen in Table 3.1.

Table 3.1: Effect of ESC timing on motor thrust (test conducted at 0 m/s)

Timing [°]	Max Thrust [N]
3.75	14.70
15	15.17
26.25	15.72

3.1.2 Propeller tests

The competition's organization team allowed for the choice between two propeller options, namely the 'APC-E 10x6E' and the 'Aeronaut CAMcarbon Light 10"x6"'. In result of the comparative wind tunnel tests conducted by the team (see Figure 3.1), it was concluded that the 'Aeronaut CAMcarbon Light 10"x6"' performed slightly better for low air velocities, while the 'APC-E' was superior for higher speeds. Since the aircraft will perform most of its flight's duration at velocities higher than 10 m/s, the 'APC-E 10x6E' was chosen. Given that the difference is almost negligible, this decision may be revisited after future flight tests.

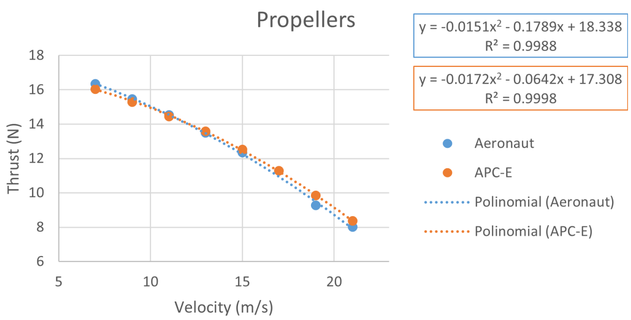

Figure 3.1: Thrust as a function of velocity using a voltage source for both propellers

3.1.3 Battery capacity

The initial estimates, based on the operating voltage and current of the motor present in its data-sheet, pointed to the need for a battery with a capacity of around 2800 mAh in order to accomplish the mission. This led to the first wind tunnel tests being conducted using this battery (Figure 3.2a).

After this test, a very significant decrease in the thrust generated was noted, to such an extent that it had dropped to half after 3 minutes. These results motivated further tests on the other 3 batteries available - one with 4000 mAh capacity, one with 5000 mAh and one with 8500 mAh (see Figure 3.2b). This time, they were conducted at 9 m/s.

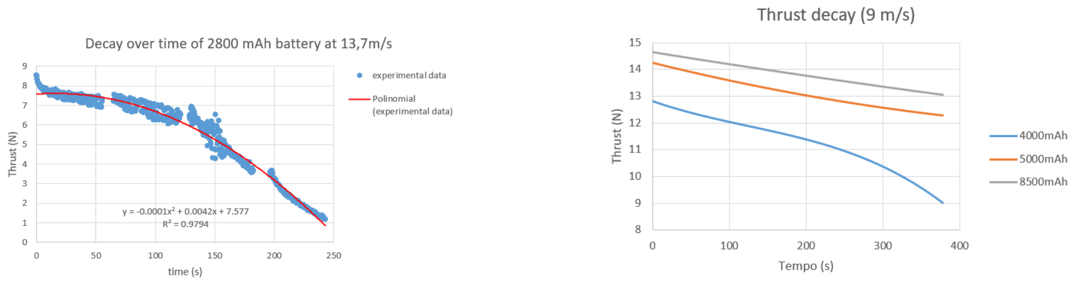

(a) Thrust decay using 2800 mAh battery **(b)** Thrust decay for 3 different batteries

Figure 3.2: Time decay of thrust

These tests led to the conclusion not only that for a larger battery capacity the decay of thrust was lower, but also that the initial value of thrust generated is greater for batteries with bigger capacity (even though all 3 were fully charged).

Therefore, the ideal battery would have a capacity big enough not to decay too much but not too big as to unnecessarily increase the weight. Therefore, the chosen battery was one with a capacity of 5000 mAh ('Gens Ace 5000mAh 3S 11.1V 50C - Bashing Series').

3.1.4 Thrust Function (t,v)

Finally, the wind tunnel tests resulted in thrust curves for a 5000 mAh battery as a function of time for two different velocities (9 m/s and 17 m/s). Subsequently, the team developed a *MATLAB* code that takes velocity and time as inputs. It uses the functions taken from figures 3.1, 3.3a and 3.3b to extrapolate the resultant thrust and plot a 3D surface, which is presented in figure 3.3c.

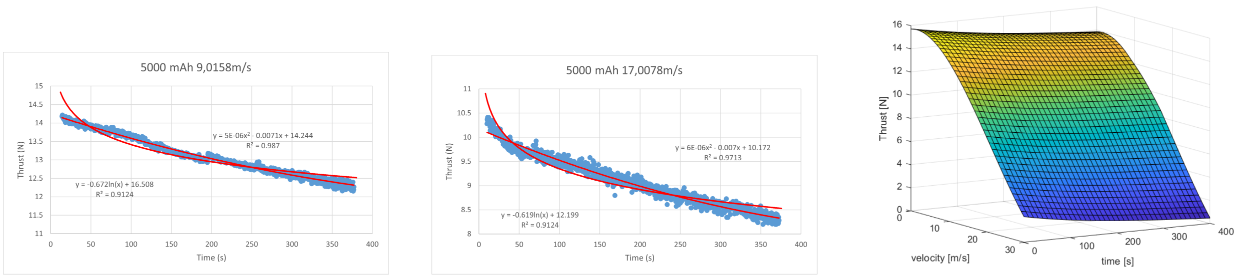

(a) Thrust decay using 5000 mAh battery for 9 m/s **(b)** Thrust decay using 5000 mAh battery for 17 m/s **(c)** Extrapolation of the results

Figure 3.3: Final results used for the aerodynamic design

3.2 Wing Design

Bearing in mind both ACC's scoring methods and size restrictions, the team developed an optimized design space program that tackles both aspects, yielding the best wing and landing gear design given the constraints. For this purpose, a *MATLAB* algorithm was developed, aiming to score each configuration out of the following variables: Aspect Ratio (AR); Wing Area (S); Height (achieved within 60 s after takeoff); Landing Gear (taildragger or tricycle); Payload.

Besides these variables, it must also be assured that not only the wing fits in the limiting rhombus-shaped box, but that a stable configuration can be built upon it, and that the final assembled plane fits in said box. As such, the design space algorithm is divided in three main segments, as follows:

- **Geometry Functions**: responsible for evaluating and scoring a specific wing given the competition's size restrictions. In other words, only wings with configurations that fit in the limiting box will be evaluated;
- **Evaluating Functions:** scoring the wing performance in terms of the five main variables listed above;
- **Data Compilation**: plots a 3D surface, figure 3.4 where the score (the more negative the better) will be plotted against Aspect Ratio (AR) and Wing Area (S). The surface will be color encoded (RGB), allowing to represent the three extra variables:

  Landing Gear: Taildragger - green; Tricycle - red;

  Payload: Greater payload increases the amount of blue;

  Height: Greater height increases the amount of green.

  In addition to data plotting, a gradient function finds the optimum design point - the point with the greatest absolute value of score.

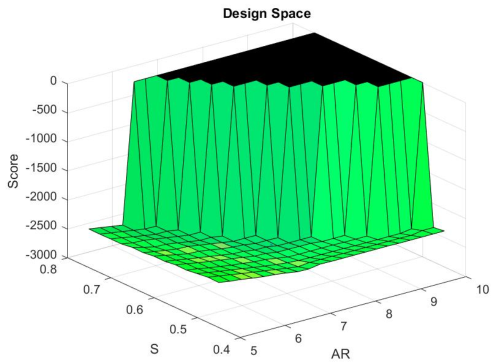

Figure 3.4: Wing scoring with the design space

The final wing design is a taildragger configuration and, prior to the winglet studies, had an aspect ratio of 7.4250 a wing area of 0.5812 m^2.

3.2.1 Geometry Functions

In this section, a specific wing configuration (AR and S pair) is tested in terms of its size and stability. The iterative algorithm, for different box angles, assesses if the wing fits the box span- and chord-wise (at the tip). It also maximizes the longitudinal distance, in order to maximize the potential distance between the aerodynamic center (AC) of the wing and the horizontal stabilizer's AC, allowing for greater stability.

After that, the algorithm calculates the area for a horizontal stabilizer capable of producing a stable configuration to check if said stabilizer also fits the box. For the horizontal stabilizer area, equation (3.2) is used [1]:

$$C_H = \frac{S_H \cdot l_H}{S_W \cdot C_{MAC}} \tag{3.1}$$

where C_H is the stability coefficient (experimentally determined to be 0.5), S_H is the tail area, l_H the distance between the aerodynamic centers (of the wing and horizontal stabilizer), s_W the area of the wing and C_{MAC} the mean aerodynamic chord of the wing.

If the horizontal stabilizer doesn't fit in the limiting box, the wing will be deemed unusable, otherwise said configuration's performance will be evaluated (and scored) in the next section.

3.2.2 Evaluating Functions

For each set of the 5 previous mentioned independent variables, this section utilizes auxiliary functions to calculate the remaining dependent variables: K-factor (k); Aircraft Weight (W); Minimum Drag Coefficient (C_{D_0}); Maximum Cruise Speed (V_{Cruise}); Weight/Surface Area of the Wing (W/S).

With all these collected data, further calculations allow the team to identify the velocity which maximizes the L/D ratio, the ideal velocity to perform a turn and the climb angle. This also allows for the calculations of the total drag coefficient, using the following equation:

$$C_D = C_{D_0} + kC_L^2 \tag{3.2}$$

Note that C_{D_0} is calculated for each part of the aircraft and then summed to its total value. Most of the equations used to calculate the dependent variables consist of empirical equations from [1].

Thrust to velocity curves for each instant of the flight are used to determine if the aircraft is capable to perform the needed maneuvers, i.e., if it has enough power. If the aircraft is not able to execute one of the flight phases - Take-Off, Climb, Stall Speed (bellow 10 m/s), Cruise, Maneuvers and Landing - it is excluded.

Each set of independent variables undergoes these successive calculation steps, which can take a long time and a lot of computational capacity, but ensures very satisfactory results. In addition, there's an implemented function in this program which takes all this data to solve for a simple AR and S input and returns both the best score possible as the characteristics needed to achieve it. Once all the relevant information about each configuration is gathered, each AR and S point are given a punctuation and ranked taking into account the ACC's scoring methods. The best configuration is then chosen. Finally, the initial design point is chosen, and it's ready for the following design steps.

3.3 Payload Prediction

The payload prediction can be divided into two phases: the first one carried throughout the wing design optimization, and the second one afterwards, once the design of the total aircraft is in its final stages, by making a detailed evaluation of whether the wing design choice was able to take off.

Starting with the criteria used in the wing design optimization, the program checked if the configurations had enough power to complete climb, take-off for 40 m, take-off for 60 m, cruise and other maneuvers.

The formulas used for the power required at each stage were the following [1]:

$$P_{climb} = \frac{1}{\eta_{climb}} \cdot (RC + \frac{q \cdot C_{D_0} \cdot V_H}{W \cdot S} + W \cdot S \cdot \frac{V_H}{q \cdot \pi \cdot AR}), \tag{3.3}$$

where η is the propeller efficiency, which was equal to 0.8 for the climb stage, RC is the rate of climb, q is the dynamic pressure, V_H is the horizontal speed, W is the weight, S is the area and AR is the aspect ratio;

$$P_{TO} = \frac{1}{\eta_{TO}} \cdot \frac{V_{TO}}{\sqrt{2}} \cdot (\frac{V_{TO}^2}{2 \cdot g \cdot d_{TO}} + q \cdot \frac{C_{D_{TO}}}{W \cdot S} + \mu(1 - \frac{q \cdot C_{L_{TO}}}{W \cdot S})), \quad (3.4)$$

where $\eta_{TO} = 0.8$, d_{TO} is the take-off distance (either 40 m or 60 m);

$$P_{cruise} = \frac{1}{\eta_{cruise}} \cdot (\frac{\rho \cdot V^3 \cdot C_{D_0}}{2 \cdot W \cdot S} + \frac{2 \cdot k \cdot W \cdot S}{\rho \cdot V}), \quad (3.5)$$

where $\eta_{cruise} = 1$, k is the k factor, equal to $\frac{1}{\pi \cdot e \cdot AR}$, where e is the Oswald coefficient;

$$P_{turn} = \frac{1}{\eta_{turn}} \cdot (\frac{\rho \cdot V^3 \cdot C_{D_0}}{2 \cdot W \cdot S} + \frac{2 \cdot k \cdot n^2}{\rho \cdot V} \cdot W \cdot S), \quad (3.6)$$

where $\eta_{turn} = 0.8$ n is the load factor, equal to $\frac{1}{cos(\phi)}$, where ϕ is the bank angle, equal to $arctg(\frac{V^2}{g \cdot R_{turn}})$, where $R_{turn} = 25$m.

Moving to the take-off study, this program can once again be divided into two parts: checking if the tail is capable of leaving the ground and checking if the airplane is capable of completing the take-off in 40 m, because the selected configuration by the program was both a taildragger and predicted to take-off in 40 m.

The first part is completed by solving two equations: the sum of forces in the Z axis (equation 3.7) and the sum of moments in the CG of the airplane (equation 3.8) [1]. Since in the early flight stages the aircraft is moving horizontally and not rotating, both of the previous values are equal to zero. The meaning of each term in the following 4 equations can be seen in Figure C.1 from **Annex C**.

$$\sum F_Z = 0 \Rightarrow R_M + R_T + L_W - W + L_{HT} = 0 \quad (3.7)$$

$$\sum M_{CG} = 0 \Rightarrow -Ty_T + R_M x_M - L_W x_W - R_T x_T - L_{HT} l_{HT} - \mu \left(R_M + R_T\right) h_{CG} + M_W = 0 \quad (3.8)$$

These equations are solved to find out the velocity at which the tail of the airplane leaves the ground, i.e., at what velocity the reaction force of the wheel in the tail is equal to zero. The resulted is then integrated, using Newton's Second Law in the x axis, to find out at what distance from the starting point, the tail of the airplane leaves the ground.

The second part is executed by calculating the required velocity for the airplane to complete the take-off, that meaning, when the Lift is equal to the Weight of the aircraft (eq. 3.9). This value is then multiplied by 1.2 for safety measures. Then, the program finds the velocity that the aircraft achieves at 40 m, by solving the differential equation that defines the system, with the starting point being the instant when the tail left the ground (equation 3.10). This program enabled the conclusion that the aircraft was capable of taking off in 40 m.

$$L = W \iff \frac{\rho}{2} S v^2 C_L = mg \iff v = \sqrt{\frac{2mg}{\rho S C_L}} \quad (3.9)$$

$$\sum F_x = m\ddot{x} \iff \ddot{x} = \frac{T_2 \dot{x}^2 + T_1 \dot{x} + x + T_0 - \mu mg + \frac{\rho}{2} S \dot{x}^2 (\mu C_L - C_D)}{m} \quad (3.10)$$

3.3.1 Payload vs Air Density

To determine the correlation between the payload prediction and the air density, the team used the program described in Section 3.3 to study the take-off, since this is believed to be the part of the flight that is the most affected by changes in the payload.

One of the program's parameters was the air density, ρ, thus, this value was changed to determine the maximum payload that the aircraft could carry while completing the take-off. To determine which values of ρ were worth experimenting with, the following formula was used: $\rho = \frac{p}{RT}$. In order to assess the atmospheric pressure, p, and temperature, T, last competition's values in Munich provided a reliable example - the pressure was equal to 101500 Pa [2] and the temperature ranged from 16°C to 27°C [3], being extended to 10°C to 30°C as a safety measure. This yielded a range for ρ from 1.15 to 1.25 kg/m^3.

The results obtained can be seen in Figure 3.5, and the formula is as follows:

$$\texttt{payload\_prediction}(\rho) = \begin{cases} 1.96 \cdot \rho + 0.048, & \text{if } \rho < 1.2 \\ 2.4, & \text{if } \rho \geq 1.2 \end{cases}$$

The values after $\rho = 2.4$ are constant, since the cargo-bay does not have the volume to hold more than 8 bags. Note that the value in the function is always a maximum, so, for each value of ρ, the results need to be truncated according to the number of blood bags.

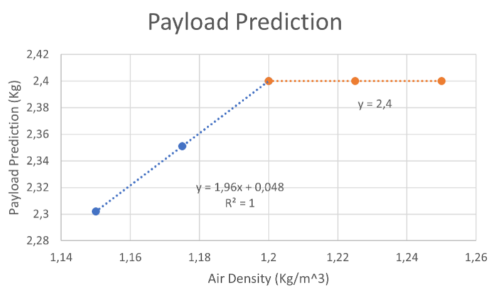

Figure 3.5: Payload prediction depending on air density

3.4 Airfoil Design

Rather than using existing airfoils in this competition, the team decided to develop its own airfoil which would meet the requirements set out by the wing design. To do so, a genetic algorithmic optimization was developed. Even though the main functioning scheme is similar to all genetic algorithms, both the reproduction and fitness function were challenges.

The reproduction was overcome with the introduction of control points, as seen in figure 3.6a, determined using Chebyshev nodes. It was conducted by mixing the points, with random small variations, from different elements of the population. Despite making the process of reproduction easier, this method created the problem of having to reconstruct the airfoil using only 11 points. That was overcome with an Akima Interpolation and a smoothing filer. Even though some detail from the input airfoils is lost, for the optimization, this method works satisfactorily.

The fitness function uses Xfoil analysis as a base. Initially it was fixed on a point's C_L/C_D but that approach minimized C_D and excessively increased C_L, producing odd shapes. The superior method was found to be estimating the take-off, cruise and climb angles, and using sigmoid functions, exemplified in figure 3.6b. The multiplication of two mirrored sigmoid functions, seen in figure 3.6c, generates a plateau shape. C_L inside the target region return a value of 1, while C_L outside the target zone return an inferior value. When multiplying the return values of several functions, for take-off, cruise and climb, with the C_L/C_D, the program had the intended tendency to reduce C_D at the selected C_L.

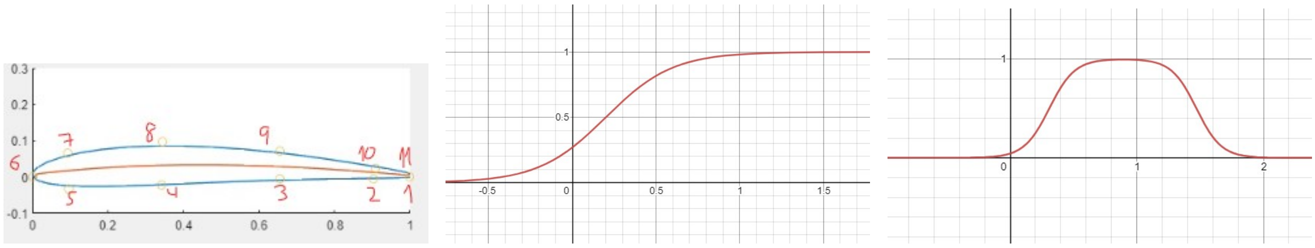

(a) Control points **(b)** Sigmoid function **(c)** Two sigmoid function multiplied

Figure 3.6: Control points and functions used as fitness functions

After defining the fitness function, multiple analyses were run. The best airfoils were shortlisted and tested in the real wing using XFLR5. The C_L/C_D curves of the wing were useful to compare the airfoils which had the least C_D for the predicted C_L values of cruise. This resulted in the choice of two airfoils. Their respective pictures can be seen in figure 3.7, and their data sheets are in tables D.1 and D.2 from **Annex D**.

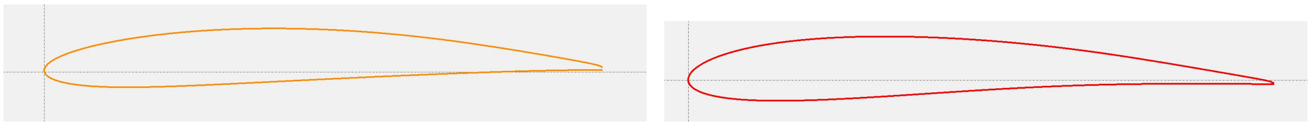

(a) Airfoil at the tip **(b)** Airfoil at the root

Figure 3.7: Final choices for the airfoils

The team chose two airfoils to achieve aerodynamic twist, with the airfoil that entered stall for higher angles of attack at the tip, and the airfoil with the higher peak of C_L/C_D at the root, as it can be seen in figure 3.8. Also note that the selected airfoils have higher C_L/C_D ratios for the angles typically used in cruise, when compared to commonly used ones.

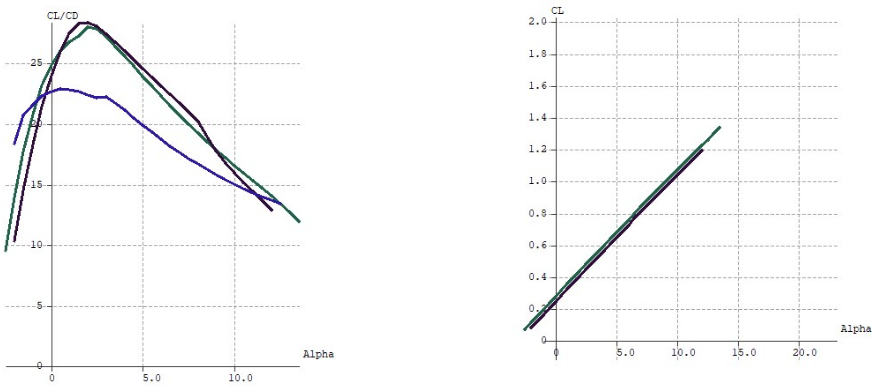

(a) Higher CL/CD for angles typically used in cruise **(b)** Wing tip airfoil has a higher stall angle

Figure 3.8: Relevant polars for the wing tip airfoil (green), wing root airfoil (brown) and NACA6410 (blue)

3.5 Tail Design and Stability

The main concern in designing the tail of the aircraft is the stability, but other requirements were also considered. To check that the aircraft was stable (the most important requirement) but not excessively, compromising pilot control, the following references were used:

Table 3.2: Reference values [4].

Stability	Parameter	Optimum Values
Longitudinal Static	Static margin [%] C_{m_α} [/º]	5 to 15 -0.01745 to -0.01047
Lateral Static	C_{l_β} [/º] C_{n_β} [/º]	-0.00349 to -0.000873 0.000873 to 0.00349
Longitudinal Dynamic - Phugoid	Damping Coefficient	> 0.02
Longitudinal Dynamic - Short Period	Damping Coefficient	0.35 to 1.3
Lateral Dynamic - Spiral	T_2 [s]	> 8
Lateral Dynamic - Rolling	$\mathcal{T}$ [s]	< 1.4
Lateral Dynamic - Dutch Roll	Damping Coefficient Natural Frequency (Hz)	> 0.08 > 0.079577

Another requirement for the tail was its fitting in the limiting box along with the assembled aircraft. In order to be absolutely sure that there were no faults in this issue, a CAD representation of the box was made with the aircraft and changed all the necessary parameters of the tail in each design. Using this CAD, it was possible to ensure that, for each configuration, the distance between the aerodynamic center of the tail and the CG was as large as possible, while still fitting in the box, in order to increase the lever arm. This is important as it allows the reducing of the dimensions of the tail and consequently the drag caused by it.

Once the first step of defining the requirements was concluded, several tails were designed and analyzed in *XFLR5*, the first ones being conventional "T" tails, already assembled with the wing. For each tail, all the requirements defined in table 3.2 were checked, until the one that had the best aerodynamic characteristics stood out, while achieving these objectives, especially in terms of lift and drag coefficients, velocity and angle of attack.

Taking this most effective "T" tail as a first draft, the team developed a "V-tail" configuration that would allow a reduction of drag, while trying to maintain the stability and control parameters. This was again an iteration problem, in which the first approach was "converting" the T-tail into an equivalent V-tail. This tail had an angle in relation to the horizontal plane, in such a way that the horizontal and vertical projections of the tail were respectively equivalent to the horizontal and vertical stabilizers of the T-tail. Then, once more, several tails were designed, with small variations in different geometric parameters, and compared, until the best one was found, according to the previously detailed objectives.

The final step was to convert the geometry into an elliptical tail, in order to reduce the induced drag. To do this conversion, there is an equation that provides the chord as a function of the distance to the root of the tail, expressed in equation (3.11):

$$c(y) = \frac{1}{2}\left(\frac{4S}{\pi b}\sqrt{1-\left(\frac{2y}{b}\right)^2} + \bar{c}\right) \tag{3.11}$$

The tail that was finally achieved, not only met all the imposed requirements with regard to stability, being all the parameters inside or close to the defined boundaries, but also provided good aerodynamic results. Regarding the first statement, the values by which it is characterized are as follows:

Table 3.3: Values obtained with XFLR5.

Stability	Parameter	Value
Longitudinal Static	Static margin (%)	9.29
	C_{m_α} (/º)	-0.0102
Lateral Static	C_{l_β} (/º)	-0.000495
	C_{n_β} (/º)	0.000939
Longitudinal Dynamic - Phugoid	Damping Coefficient	0.022
Longitudinal Dynamic - Short Period	Damping Coefficient	0.643
Lateral Dynamic - Spiral	T_2 (s)	9.006
Lateral Dynamic - Rolling	$\mathcal{T}$ (s)	0.022
Lateral Dynamic - Dutch Roll	Damping Coefficient	0.143
	Natural Frequency (Hz)	0.885

By comparing tables 3.2 and 3.3, it can be concluded that almost all parameters are within the desired range. The exceptions to this conclusion are $C_{m\alpha}$, which is lower, in terms of absolute value, than the target value, and $C_{l\beta}$ which is much lower, although not as impactful as the former. Despite these exceptions, this was the tail we were able to draw that was a better trade-off, considering the stability, the external impositions, the reduction of drag and the additional difficulties of designing a V-tail.

The same analysis was done for the possible extreme positions of the CG. These extreme positions define the range of values between which the longitudinal stability is guaranteed, with the angle of attack at the equilibrium point being lower than 3°. They were found in XFLR5 and correspond to static margins of 8.2143% and 12.5%. The results are presented in table 3.4.

Table 3.4: Values obtained with XFLR5 for the extreme positions of the CG.

Stability	Parameter	Value	Value
Longitudinal Static	Static margin (%)	8.2143	12.5
	C_{m_α} (/º)	-0.0065613	-0.013055
Lateral Static	C_{l_β} (/º)	-0.00049	-0.000411
	C_{n_β} (/º)	0.000935	0.000952
Longitudinal Dynamic - Phugoid	Damping Coefficient	0.018	0.034
Longitudinal Dynamic - Short Period	Damping Coefficient	0.655	0.602
Lateral Dynamic - Spiral	T_2 (s)	7.93	13.397
Lateral Dynamic - Rolling	$\mathcal{T}$ (s)	0.034	0.028
Lateral Dynamic - Dutch Roll	Damping Coefficient	0.149	0.134
	Natural Frequency (Hz)	0.851	1.037

To conclude this section, the values obtained for the extreme positions of the CG show that, for the lower static margin, the aircraft can be somewhat statically unstable, with special concern in the longitudinal axis; for the higher static margin, static stability is ensured, with the exception of the C_{l_β} derivative, which remains too low. Regarding dynamic stability, all the parameters fit almost perfectly in the desired ranges for both extreme positions.

3.6 Control Surface Design

For the sizing of the control surfaces of the aircraft, the team calculated the theoretical values needed, using as parameters the values taken from the wind tunnel tests.

The aileron size has two dimensions - width and length. The width of the aileron was set to 25% of the length of the chord on the surface midpoint, as it's a typical and acceptable value for this parameter, based on team experience. On the other hand, for the value of the length of the ailerons, other calculations were made.

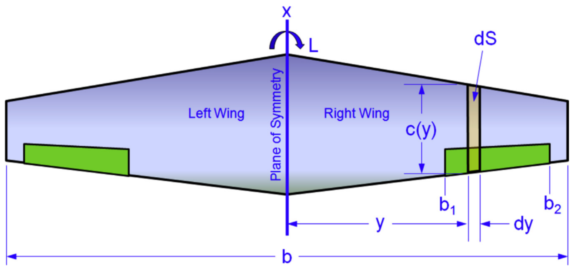

Figure 3.9: Aileron design variables

The parameter used to evaluate the performance of the ailerons of the aircraft is the roll helix angle ($\frac{pb}{2V}$). This factor takes into account two important aspects of control surfaces: authority at low speeds and authority at high speeds. For cargo airplanes, it is recommended that this factor exceeds 0.07. Nevertheless, the team decided to aim for a 0.09 value, to ensure safety and maneuverability at more critical scenarios.

The roll helix angle depends on the aileron authority derivative, $C_{l_{\delta_a}}$, the roll damping derivative, C_{l_p}, and the maximum achievable deflection, δ_a, a relation which is established as follows:

$$\frac{pb}{2V} = -\frac{C_{\delta_a}}{C_{l_p}}\delta_a \tag{3.12}$$

The present parameters are determined by the following equations:

$$C_{l_{\delta_a}} = \frac{dC_l}{d\delta_a} = \frac{2c_{l_{\delta_a}}}{Sb}\int_{b_1}^{b_2} c(y)\cdot y\cdot dy \tag{3.13}$$

$$C_{l_p} = -\frac{4\left(c_{l_\alpha}+c_{d0}\right)}{Sb^2}\int_0^{b/2} y^2\cdot c(y)dy \tag{3.14}$$

$$\delta_a = \theta_{max}\cdot 0.75 \tag{3.15}$$

where b is the wing span, in m, S is the wing area, in m^2, b_1 is the starting point of aileron, in m, b_2 is the ending point of aileron, in m, shown in figure 3.9. θ_{max} is the maximum achievable deflection angle of the ailerons in rad. The other variables used are $c_{l_{\delta_a}}$, c_{l_α} and c_{d0}.

To obtain $c_{l_{\delta_a}}$, the team resorted to wind tunnel tests. For the change in lift coefficient with aileron deflection $c_{l_{\delta_a}}$, small deflections were studied, whose effect was then approximated as linear, extracting the $c_{l_{\delta_a}}$ value.

For c_{l_α} and c_{d0}, the team calculated the average of their values on the airfoil from the tip of the wing and the one on the root of the wing. They were both determined using XFLR5 analysis.

As for the parametric representation of the chord, $c(y)$, the equation for the elliptical wing used is the same used for the tail (equation 3.11).

The process used to optimise the size of the ailerons was an iterative one. The team used the previously known variables and varied the other ones, namely b_1, in order to get the desired value for the roll helix angle. The team also noticed that the calculations without considering the existence of the winglets were stricter, needing a bigger aileron to achieve a $\frac{pb}{2V}$ larger than 0.09, so the team chose to use these parameters. The value used for the maximum achievable deflection angle of the ailerons, θ_{max}, was 15°. The rest of the parameters that resulted from the iterative process are:

$$\begin{cases} b_1 = 0.67 \text{ m} \\ b_2 = \frac{b}{2} = \frac{2.044}{2} = 1.022 \text{ m} \\ S = 0.5812 \text{ m}^2 \\ c_{l_{\delta_a}} = 3.7455 \end{cases} \Leftrightarrow \begin{cases} \delta_a = \theta_{max} \cdot 0.75 = 15(\frac{\pi}{180}) \cdot 0.75 = 0.1963 \text{ rad} \\ C_{l_{\delta_a}} = 0.4338 \\ C_{l_p} = -0.9334 \end{cases}$$

$$\Leftrightarrow \frac{pb}{2V} = -\frac{C_{l_{\delta_a}}}{C_{l_p}}\delta_a = 0.0912 > 0.090$$

With these parameters, the ideal result is a aileron length of 0.352 m. Despite this result, the experience of the team and the fact that there was room for a bigger aileron, it was decided that it would be 0.42 m. A bigger aileron allows for more control over the airplane, needing slighter deflections to achieve equal results, which is a positive point, as bigger deflections generate greater drag.

As for the flaps, the rest of the wingspan toward the fuselage was used, applying the same width (25% of the chord on the surface midpoint). For the tail, the team decided to use the whole length of the trailing edge for the ruddervators. Their width was set to 30% of the chord, as it is a reasonable and typical value for this, according to experience.

3.7 Winglet

In order to achieve a high efficiency, the consensus was that even with an elliptical wing, a winglet could be a performance boosting design decision. As a result of some research, the team concluded that, for the mission in question and the wing in use, the winglets that were good candidates were the canted winglet, the blended winglet and the sharklet winglet. Not withstanding, the team not only considered other types of winglets like the witcomb design, but also looked into alternatives such as a polyhedral wing that, with a further inspection, showed their costs outweighed their benefits.

In order to quickly get proper results of the winglets' performances, *XFLR5* simulations were completed by modelling the various configurations and iteratively changing different parameters and measuring their effects on the wing's performance. These simulations were run for an expected interval of the aircraft's cruise velocities in *XFLR5* using the VLM model. Let it be noted that the results obtained in *XFLR5* were very optimistic, despite the approximated nature of the methods used.

The next step was to analyze the data, with an emphasis on both the Lift and Drag Coefficients, (C_L) and (C_D), as functions of the angle of attack (AOA) plots, and the Drag Polar plot, (C_L) as a function of (C_D). The best configurations were selected to simulate in CFD. The finest winglet configurations were modelled in *SolidWorks*.

This 3D model would be the geometry for the CFD simulation using *Ansys Fluent*. To evaluate the quality of the simulation methodology, these results were compared to the experimental ones, obtained by performing wind tunnel tests for a both canted and blended winglets. The results discussed in Section 3.9 for CFD precision lead to more confidence in the simulations.

The C_L/C_D ratio results, obtained for different angles of attack, revealed that the sharklet winglet has the best results, followed by the blended winglet. The final winglet designs can be seen in figure 3.10.

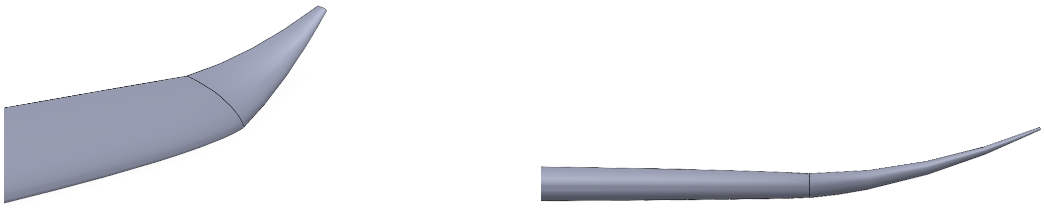

(a) Isometric view **(b)** Front view

Figure 3.10: Sharklet winglet CAD design in *SolidWorks*

3.8 Stall Studies

The stall study tries to as accurately as possible predict the angle of (static) stall, through the wind tunnel tests, the XFLR5 and the latest CFD results. This information reveals the aircraft's limits within which the team can operate.

Not many conclusions could be drawn from the initial wind tunnel runs, they were not planed with this intent. This led to the exclusive testing of wings at -10° to 15° of angle of attack, leaving little data around 14° and 15° for the stall region to be well analyzed.

Secondly, through *XFLR5* simulation with the VLM2 model, a stall angle between 12° and 13° was obtained. Although this was not the angle of maximum lift coefficient, it was the angle at which the lift coefficient stopped being proportional to the angle of attack, which we consider to be close to the stall angle.

Lastly, steady CFD simulations were executed using different AOAs, starting at the *XFLR5* predicted values 12° and 13° and increasing them. The team then concluded, through post-processing, that the stall angle was 26° - the angle at which the wing root entered a stall state. Even though this obtained value doesn't seem to correspond to the real one, evidences showed that the stall started at the root, span-wise to the tip, as illustrated in fig. 3.11. This guarantees that the control surfaces are working when the wing starts to stall. A later wind tunnel model, discussed in Section 3.9, would confirm that the stall is happening at around 14,5°, confirming the team's suspicions.

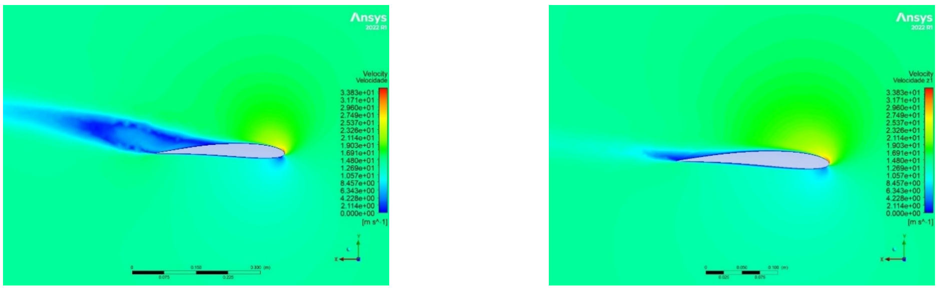

(a) Wing root **(b)** Near the wing tip

Figure 3.11: Velocity contours of airflow around sections of the wing at an angle of attack of 26° obtained in *Ansys Fluent*

In terms of the dynamic stall, no simulations were executed for a projection: in *XFLR5* these results are impossible to obtain, but the wind tunnel and the CFD results deem themselves satisfactory, motivating further investigation in this area.

3.9 Wind Tunnel Testing

During the development of the aircraft, the team had the opportunity to use the wind tunnel at the Portuguese Air Force Base nº1, in Sintra, 3 times, with 3 different models and 4 different objectives. The first one was to verify first hand the models used. In figure 3.12a the wind tunnel data was compared with 2 drag polar models. Even though the C_{D_0} estimations were on point, the simpler model's reliability was a surprise, and the team ended up choosing it over the more complicated one. Note that the model was not elliptical, but had similar characteristics to the aircraft's design, such as the aspect ratio and area. The models were applied to the simpler design in order to be tested. In these experiments, a smaller scale model of the wing was used, maintaining the same Reynolds number, by performing tests at higher wing speeds according to the scale factor.

For the second time, emphasis was given on surface deflection, to gather experimental data with the genetically created airfoil for aileron design. This model was also the one implemented to test different winglets (e.g. figure 3.12b). Besides comparing the winglets between themselves, the wind tunnel data was compared to that of the CFD. The C_D value obtained in the wind tunnel doesn't include the central section's contribution, so the simulated C_D was expected to be slightly higher. Even though the results were off by around 10% in C_D and 20% in C_L the same tendencies were observed. The winglets that performed better in the wind tunnel had the exact same performance difference in the simulations. This lead to confidence in the utilized Viscous Model (k-epsilon - Realizable - Non-equilibrium Wall Functions), specially on how they were applied. The CFD was not used to gather precise data, but rather as a method to compare designs from then on.

The last model was focused on performance evaluation. For this, the real final design of the aircraft was established, as seen in figure 3.12c, instead of a simplified model. This allowed for some drag related items to be tested. It was found that covering the surface of the wheels had an impact on drag of around 4.5%. The main intent though was to gather accurate C_L, C_D and C_m data, with different flap and aileron angles, to estimate the optimum deflections at take-off, climb and cruise, for maximum speed at different payloads. With this data, it was also confirmed that the wing stalled at around 14.5°, as shown in Section 3.8.

(a) Model testing

(b) Scale model of the wing with the canted winglet in the wind tunnel

(c) Wind tunnel performance evaluation

Figure 3.12: Different applications of wind tunnel tests

3.10 Fuselage

The aerodynamic shape of the fuselage was achieved having in consideration all the different components it must accommodate; not only the payload, but also the electronic components, the GPS and all the connection elements between the various parts of the aircraft. The change in this competition's regulation led us to define new goals, specially regarding the volume needed inside the fuselage, given the large dimensions of the blood bags, so a great care was taken to ensure every other element would fit inside the fuselage.

The most important details to address in order to improve the fuselage's aerodynamic performance were: tangentially joining the wings and fuselage; the sharp angle given in the empennage portion; the large frontal area (compared to the total length); and the body's rough surface.

The CFD analysis which compared different designs (Figures 3.13a and 3.13b) allowed for the conclusion that the major factor increasing drag was the frontal area of the fuselage. This led the team to reduce the height and width of the body to a bare minimum through a 4×2 bag configuration, with 4 columns of 2 bags each, leaving only a small gap as margin. Furthermore, the electronic components' section was condensed. Since this is carried in the foremost part of the fuselage, its volume is crucial to determine the path of the air around the body and its interaction with the wings. Besides this, the team aimed to maintain an acceptable body length vs frontal area ratio (in values above 5), while restricting the additional friction drag.

(a) Half circular fuselage - *L/D = 16.640 (Full Fuselage)*

(b) Half squarish fuselage - *L/D = 17.302 (Full Fuselage)*

Figure 3.13: CFD study designs in *SolidWorks*

In the CAD design (Figure 3.14a), the tangency between the airfoil and the cargo-bay was ensured, as well as a reduced angle in the empennage zone. These characteristics allow a better lift generation, keeping the airflow aligned with the wings and avoiding big separation zones (and vortices) in the rear of the fuselage, which would affect the control efficiency of the tail surfaces. Although this value was not verifiable, the airplane's stall angle predictions

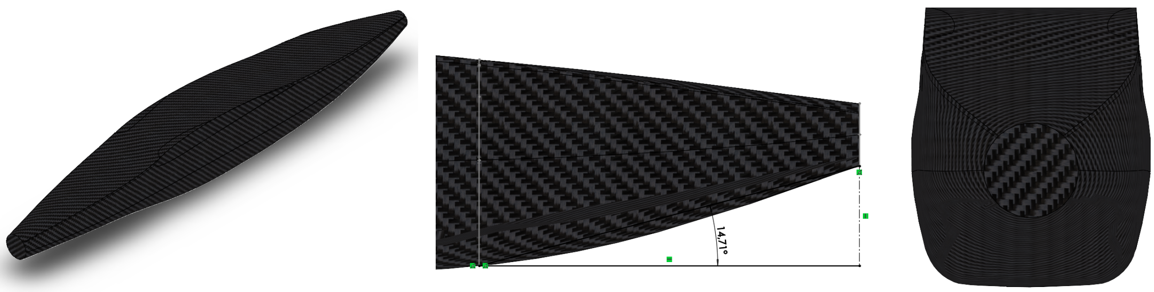

(a) Fuselage

(b) Empennage angle

(c) Frontal Area

Figure 3.14: Fuselage CAD design in *SolidWorks*

based on computer simulations and previous models showed a stall angle of approximately 15°. For this reason, the empennage angle was set around this value (Figure 3.14b).

Finally, having a smooth surface would decrease the fuselage's friction drag, so the team used appropriate construction methods to achieve this, as explored in section 4.3.

3.11 Landing Gear Configuration

To determine the height of the landing gear, the team started by finding out the limits of how much the center of gravity (CG) could be moved forward or backward without falling out of the appropriate static margin. The limits set up for these criteria were between 5% and 15%. The results were that the CG could be between x = 0.103 m and x = 0.132 m, where x = 0 m is the leading edge of the wing and x is positive in the direction of the tail. It was also assumed that the CG was the highest possible, that is, in the same plane as the wing, for extra safety.

For the forward most point, a line with a slope equal to tan$(75 \cdot \frac{\pi}{180})$ was drawn, and, for the most backward point, a line with a slope equal to tan$(65 \cdot \frac{\pi}{180})$ was drawn. These two lines intersect where the landing gear, wheel and floor intersect. This resulted in the landing gear being placed 7 cm behind the leading edge of the wing and at an initial angle of attack for the airplane equal to 9.15°, an objective which was accomplished by the addition of a small wheel below the tail, shown in sectioon 4.4.3.

The height of the landing gear was determined by ensuring that, with the airplane parallel to the ground, the distance between the propeller and the floor was 5 cm. The width of the landing gear was determined by making the angle between the line that contains the assumed CG and the wheel and the vertical axis equal to 30°. Thus, to sum up, the landing gear's final dimensions are 67 mm in height and 306 mm in width.

4 Structural Design

4.1 Wing

The wing follows a typical wing structure with spars, ribs and a shell. It's divided in two sections, both connected to the fuselage when assembled, to meet the transportation box size requirements. It has a semi-elliptical shape to ease the construction of ailerons and flaps, and winglets that are not separable from the rest of the wing. Almost all the components of the wing structure were made out of sandwich composites and studied together to optimise the stiffness-to-weight ratio, as will be explained later. Figure 4.1 shows the overall design of the right side of the wing (left side is symmetric).

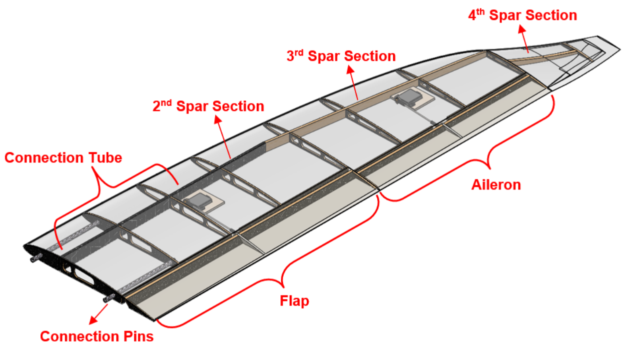

Figure 4.1: Isometric view of the rigth wing in *SolidWorks*

4.1.1 Spar and Connection

The spar accounts for sustaining the majority of the stresses from bending and torsion. Therefore, it's the stiffest component of the wing. It has a rectangular section which, when compared to a circular section, is more efficient in resisting bending stresses (the most significant on the wing), since the inertia moment is higher for the same section area. It's also easy to manufacture with composite materials and it's simple to connect with the fuselage.

The material chosen to build the spar was balsa wood wrapped in low density CFRP (Carbon Fiber Reinforced Polymer) with $90g/m^2$. This allows stiffness variation of the spar across the span, by increasing or decreasing the number of carbon fibre layers. According to our optimization results, the spar is divided in 3 sections, varying from 3 layers on the root (where the stresses are higher), to 0 layers on the tip. There is also a secondary spar that closes the division between the control surfaces and the rest of the wing.

In order to reduce weight and avoid additional parts, the main spar is used as a connection between the two halves of the wing and the fuselage. Therefore, there's a central section of the spar that connects to the CFRP 30 cm long rectangular tubes by friction and passes through the fuselage between them, as shown in figure 4.2. This removable section of the spar works like a fuse because it can be replaced easily and breaks before the rest of the wing structure (which is subject to higher stresses). The central section also defines and ensures the dihedral angle of the wing, assuming a critical role in the aerodynamic performance of the wing.

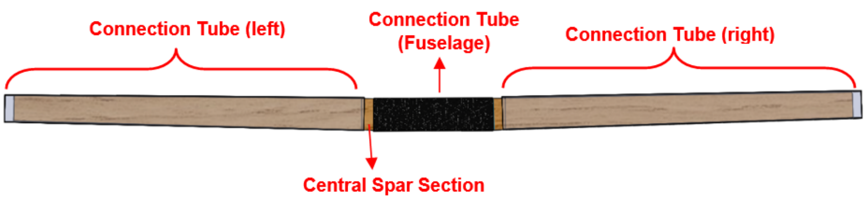

Figure 4.2: Simplified connection between wing and fuselage in *SolidWorks*

Lastly, to reduce the torsion on the connections, there are two CFRP circular tubes passing through the first two ribs and fixed by friction to 3D printed parts on the fuselage.

4.1.2 Ribs

The wing ribs serve the crucial role of preventing shell deflection further than an established value that would jeopardise its aerodynamic performance. Since it's fixed with epoxy resin to both the spars and the shell surfaces, it allows loads to be transferred between these two components.

To find a thickness and geometry of the ribs that minimizes their weight, a program of topological optimization was developed from scratch. This program generates a 2D trian-

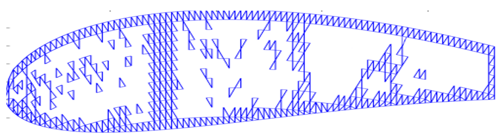

(a) 2D mesh in *MATLAB*

(b) CAD design in *SolidWorks*

Figure 4.3: Best result obtained with the ribs' optimisation program and CAD design

gular mesh to define the geometry of the rib and optimizes it by removing elements of the mesh, using an evolutionary algorithm [5] and FEM theory to determine the strength of the ribs at each iteration, based on loads computed with Xfoil. Figure 4.3 shows the best result achieved.

The ribs were cut out of a composite sandwich panel of balsa wood and one layer of CFRP, with a total thickness of 3mm. The wing contains 9 ribs with non-uniform spacing. Their position was defined according to the optimization results in section 4.1.5.

4.1.3 Shell

The shell is responsible for generating the lift force that sustains the aircraft, therefore, it's crucial to ensure that it has great dimensional accuracy and doesn't deform too much. The flaps and ailerons mechanisms were also placed inside the wing to improve its aerodynamic efficiency. Furthermore, being the largest surface of the UAV, the shell makes up about 50% of the weight of the wing (excluding servo mechanisms). Keeping that in mind, the shell is made from a thin composite sandwich, so the wing can be extremely lightweight and still achieve an acceptable strength.

This composite sandwich material is made of one layer of fiberglass and epoxy resin facings and a 1.2 mm thick foam core (*Airex®*). The shell supports a significant amount of shear stresses, so the fiberglass woven was placed at 45°/-45° to reduce wing torsion. It was also reinforced with a low density unidirectional carbon fiber in the position of the spar, to increase bending stiffness in this critical area.

4.1.4 Preliminary Optimisation

The optimisation of the overall structure of the wing was made in 2 steps: running a program developed by the team to quickly analyse a variety of solutions (preliminary optimisation); and then performing FEM (Finite Element Method) analysis to the best solution, to further understand the stresses imposed, and to reduce its weight.

For the first step, a *MATLAB* program was developed to look for a combination of parameters and perform a multi-variable optimisation, using a simple steepest descent algorithm. These parameters are coded in arrays, so they can vary along the span. The moments and torsion applied in the wing decrease closer to the wing tip, so the algorithm naturally starts decreasing its stiffness away from the root.

The program reads the output file of *XFLR5*, that contains 2D information about the forces acting on the wing surface, and computes all the bending moments and shear forces in several sections of the span. Assuming the wing section is a closed section beam with 2 cells, bending and shear stresses acting on it are computed, using analytical formulas [6]. Finally, at each iteration of the algorithm, the critical stresses are computed to determine if the spar and shell fails. On this step, the Classical Lamination Theory (CLT) [7], and the Tsai-Wu failure criteria were used.

Table 4.1: Best result from the preliminary optimization

-	0-24cm	24-47cm	47-51cm	51-86cm	86-96cm	96-111cm
Spar CFRP layers (0°/90°)	4	4	3	2	1	0
Shell Thickness	2mm	1.2mm	1.2mm	1.2mm	1.2mm	1.2mm
Shell FG layers (+45°/-45°)	1	1	1	1	1	1
Spar position	$\approx 25\%$	$\approx 25\%$	$\approx 25\%$	$\approx 25\%$	$\approx 25\%$	$\approx 25\%$

Results from this preliminary optimisation, with an estimated mass of 840 g, can be found in Table 4.1, where the upper row contains sections of the wing with constant properties, and the first column contain the optimized variables.

4.1.5 FEM Analysis

The preliminary results, allowed the wing to be optimised to a greater extent using Abaqus, a commercial FEM program. All simulations were made using both a cruise stage (with a load factor equal to 4) and a loaded climb stage with mapped pressure given by *XFLR5* and *Xfoil* simulations. Shell elements were used for the mesh, and the mechanical properties used are defined in tables E.1 and E.2, from **Annex E**. For the boundary conditions, the central section of the spar and the pinholes in the first rib were fixed.

The post-processing of the results was based on Hashin and von-Mises failure criteria. For isotropic (MoS_I) and composite materials (MoS_C), the following expressions for margin of safety were applied. Every margin of safety should be positive.

$$MoS_I = \frac{\sigma_{VM}}{\sigma_y K_P K_M K_{LD} FoS_y} - 1 \quad (4.1)$$

$$MoS_C = \frac{SR}{K_P K_M K_{LD} FoS_y} - 1 \quad (4.2)$$

where SR is the strength ratio associated with the Hashin failure criteria, σ_y is the yield strength, σ_{VM} is the Von Mises' stress, K_P is the project factor and takes into account the maturity of the design, K_M is the model factor and takes into account how representative the models used are, the yield design factors of safety, FoS_y, and the local design factor, K_{LD}, are used in series, wherein the latter takes into account local discontinuities with FoS_y (e.g. a joint), as specified by the ECSS-E-ST-32-10C standard. The values used were: $K_P = 1.2$, $K_M = 1.2$, $K_{LD} = 1$ and $FoS_y = 1.1$. Safety margins obtained are shown in **Annex E**.

The spar was designed to meet the requirements of positive margin of safety at every point. Additionally, the wing's deflection should be as uniform as possible, that means that each section of the wing should deflect about the same amount instead of the deflection being focused mostly on the root, in order to avoid over dimensioning the spar sections further away from the root. Results are shown in figure 4.4 and translate to a maximum deflection (at the tip) of about $3cm$ in a cruise situation and $9cm$ in a climb situation.

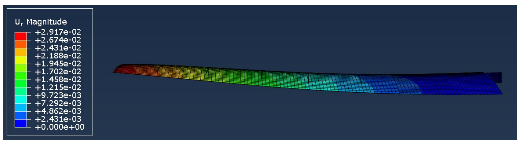

(a) Cruise

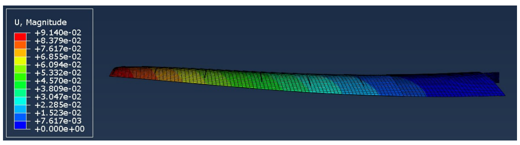

(b) Climb

Figure 4.4: Wing deflection obtained in *Abaqus* for climb and cruise

Finally, the shell was optimized much like the spar, analysing the criteria observance, using different layups made of GFRP (glass fiber reinforced plastic) woven plies as well as different core thicknesses. The number of ribs and their positions were chosen to prevent a deformation in each shell section (the area between two ribs) greater than 0.4 mm (value based on previous experience).

The final results are shown in **annex F**. Comparing to the preliminary analysis, the spar suffered a reduction of CFRP layers, and the section without carbon fiber reinforcement was increased. The shell thickness was fixed at 1.2 mm throughout the entire span, without the need for a 2mm section on the root. It was determined that only 9 ribs were needed, wherein the last ones ought to more space than the ones near the root (see Figure 4.5).

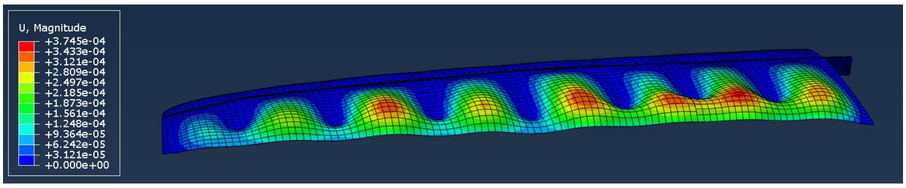

Figure 4.5: Airfoil deformation field obtained in *Abaqus*

4.2 Tail and Tailboom

Similarly to the structural design of the wing, great attention was taken to the V-tail's stiffness-to-weight ratio. To optimise this parameter, the stabilizers were built using a sandwich composite structure (the same as the one used in the wing).

As usually recommended for common aircraft, the internal structure's design consists of ribs and spars (besides the electrical components), which provide the required rigidity to the outer shell and proper load distribution along the span and chord of the stabilizers, as visible in Figure 4.6.

Figure 4.6: External and internal structure of the stabilizers in *SolidWorks*

4.2.1 Internal Structure

Spar

The spar is made from a CFRP tube with an outside diameter of 7 mm and a 2 mm thickness. To avoid intersection of the spars at the tailboom, these are offset by a distance of 10 mm, being the centerline of the two spars located at 25% of the stabilizer's chord at the root. This is a bought part, manufactured using carbon fiber pultrusion and epoxy resin, making this a low weight tube highly resistant to bending at a relatively low cost when compared to other manufacturing processes, such as pullwinding.

Ribs

Firstly, the rib at the root (Figure 4.7a) contains two connections, each requiring its own specific orifice: a simple one for the spar and another directly to the tailboom via an M3 bolt, therefore containing an M3 tee-nut. In addition, there are 2 more holes, both aiming to reduce the part's weight, wherein one of them serves the purpose of allowing the passage of the electric cable from the servo motor.

The second rib (Figure 4.7b) is located at a distance of 100 mm from the root and serves the purpose of providing support to the electric actuators for the control surfaces.

(a) Rib at the root

(b) Rib at a distance of 100 mm from the root

Figure 4.7: Ribs of the stabilizer's internal structure in *SolidWorks*

The last rib is a shorter one that doesn't accompany the full length of the chord - only 30% - but serves a similar purpose, transferring the shell loads to the spar, being particularly relevant for the loads next to the tip of the stabilizer. Since these are smaller when compared to the loads at the root, this area must only be equipped to support a section of the chord, on the leading edge, opening way to the implementation of a smaller rib. To verify this design choice, a FEM analysis (using the same material properties as the wing) was conducted (Figure 4.8) showing that the use of this last rib decreased the deformation by 7% when the stabilizer is acting like a cantilever beam.

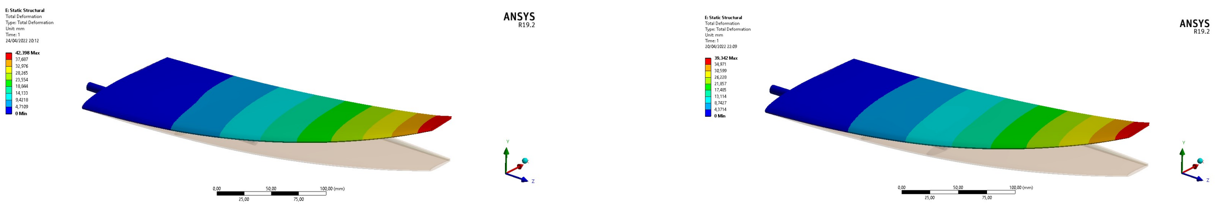

(a) Without third rib

(b) With third rib (7% less deformation at the tip)

Figure 4.8: FEM analysis of an addition of a 3rd rib in *Ansys Static Strutural*

Every rib is cut from a 3 mm thick plywood sheet using a CNC machine. This material presents itself as affordable, easy to handle and adequate to the various needs of the internal structure's components, among which stand out the nut in the rib at the root and also the servo motor's screws, which must both be safely fastened to the rib.

Regarding the electronic components, the servo motor is mounted with screws, in such a way that its cable is directly oriented to the opening in the rib at the root, as to not be blocked by the spar-connection piece.

Second Spars

Two second spars are cut from a 3 mm balsa wood sheet in order to separate the ruddervator from the stabilizer. One of these is cut perpendicular to the shell, and the other one at a 30° angle, which allows for a better rotation about the ruddervator separation axis. Moreover, these spars provide further structural reinforcement.

4.2.2 Outer Shell

The outer shell of the stabilizers is made from a composite sandwich material like that of the wing, with glass fiber, a foam core and epoxy resin - maintaining the structure's integrity, reducing weight and the need for many ribs. Note that the connection between all elements of the internal structure and the outer shell is secured using epoxy resin.

In order to meet the aerodynamics design requirements, the stabilizers intersection chord line had to be tilted by 2.5° in relation to the tailboom axis. To fulfill this, the internal structure was kept in its usual (perpendicular) position, and only the outlining of the outer shell in the building mold was tilted, exercising the same effect through a simpler application. To ensure the proper fit of the outer shell to the tailboom, an excess brim was added, which was then trimmed and adjusted.

4.2.3 Tailboom and Connection to the Stabilizers

Since all stresses applied to the stabilizer are transferred to the tailboom, the team had to employ one with reasonable size and thickness, having accordingly chosen a CFRP tube. It has an outer diameter of 25 mm and a 2 mm thickness. This tube has a matching sleeve tube with an inside diameter of 25 mm and an outside diameter of 26.5 mm that is located inside the fuselage.

After drilling the necessary holes in the tailboom, the connection of the spars, as shown in fig. 4.9, uses a 3D printed part using PETG filament, which helps not only to ensure the stabilizers are correctly positioned and but also in transferring the stresses from the spar to the tailboom's walls. There is another 3D printed part for the screw connections that ensures the head of these M3 screws are pressing on a flat surface.

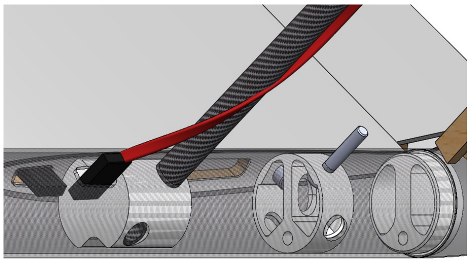

Figure 4.9: Connection of the spars to the tailboom in *SolidWorks*

The junction between the tailboom and stabilizers needed a more satisfactory fit, so a coupling piece was designed and 3D printed to rest between the root rib and the tailboom, allowing for a smooth transition between the flat surface of the rib and the curved surface of the tailboom. Finally, the end of the tailboom is capped with a cone shaped shell part to improve aerodynamic performance and the overall look of the aircraft.

4.3 Fuselage

The general shape of the fuselage was obtained with the aerodynamic performance in mind. Despite the external design already being defined, it was critical to choose what materials to use and to develop an internal structure that would accommodate the payload (bags, electronic components and the GPS) and bear the loads from the connections to the wing, the landing gear and the stabilizer.

4.3.1 Selected Materials

The most relevant factor in determining the overall structural strength of the fuselage relates to the materials employed in its construction. As the fuselage is one of the components that contributes the most to the weight of the aircraft, the material selection was crucial in optimising the specific strength.

Taking this in account, a composite sandwich material was selected for the fuselage, mainly due to its high specific strength. To determine the fiber material, the number of fiber layers employed and the core thickness, different combinations of these parameters were tested, evaluating their density and resistance to bending (qualitatively).

An ideal core to implement in the fuselage should be thin, light and flexible, adapting itself easily to the double curved geometry. A *Lantor®* textile core meets all these requirements. Distinct archetypes of *Lantor®* cores were evaluated in some test plates with different thicknesses, fiber materials, number of fiber layers as presented in Table 4.2. The relative strength of the plates was also obtained through qualitative bending tests.

Table 4.2: Materials Test Results - *Chosen combination in bold*

Core	Core Thickness (mm)	Fiber	Fiber Density (g/m^2)	Density (g/m^2)	Relative Strength
Lantor Soric® SF	3	Glass	160	925	High
Lantor Teccore® TG	1.5	Carbon	95	557	Medium
Lantor Teccore® TG	1.5	Glass	160	621	Medium
Lantor Teccore® TG	1.5	Glass	49	417	Low

The second plate was the chosen material for the fuselage. It showed a reasonable strength and was lighter than the third plate with glass fiber. Despite having higher strength, the first plate was discarded because the 3 mm core absorbed too much resin, increasing its density. Furthermore, the 3 mm core was harder to fit in the mold curved surfaces. The fourth plate appeared to be insufficient in terms of strength for the landing loads, although it was the lightest.

Finally, a simpler prototype of the fuselage was built with the chosen plate to analyse it when undergoing compression that would simulate the landing loads. This testing-based approach provided confidence to proceed with the sandwich composite material of the second row of table 4.2.

4.3.2 General Configuration

After ensuring the resistance of the outer shell, reinforcements were added to the structure (figure 4.10a) in the form of composite plates located strategically inside it. The first plate, made from a sandwich composite, is located near the wing and the landing gear connections to resist the landing impact as well as some wing connection stresses, mainly the bending. This plate is also used to separate the electronics compartment from the cargo bay. The second plate is in the rear of the fuselage, with the purpose of making the connection with the tail rod and transferring the loads to the rest of the fuselage. Besides these plates, a carbon fiber reinforcement was applied in the position of the landing gear, given the high concentrated loads in this critical section.

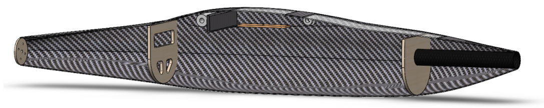

(a) Internal structure

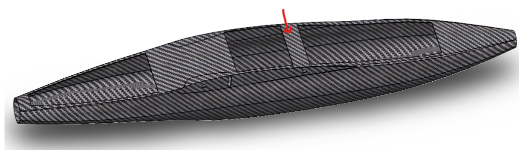

(b) Composite strip/lids

Figure 4.10: Fuselage in *SolidWorks*

The access to the inside of the fuselage is made through three lids. Their positions and sizes was set in a way that the stress concentration zone remained solid. There is one lid dedicated to the electronics box, one lid for accessing the GPS which is fixed on an wood plate and another lid for inserting the payload. Special attention was paid not to leave significant cavities in the material, as visible in figure 4.10b where a strip of material was placed between the last 2 of the aforementioned lids.

4.4 Landing Gear

4.4.1 Shape Selection

According to the dimensions mentioned in Section 3.11, the team conducted three different shapes for the landing gear, tested in *Ansys Static Structural*, as shown in figure 4.11. By submitting all the equal material shapes to the same boundary and loading conditions, it is clear that shape A has the lower deformation of the FEM simulations. The final shape of the landing gear is based on shape A as presented on figure 4.12.

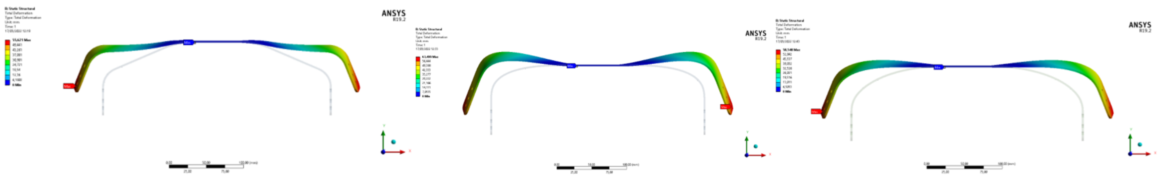

(a) Shape A **(b)** Shape B **(c)** Shape C

Figure 4.11: Deformation for 3 different landing gear shapes built from the same composite layup and subjected to the same boundary and loading conditions (in Ansys Static Structural)

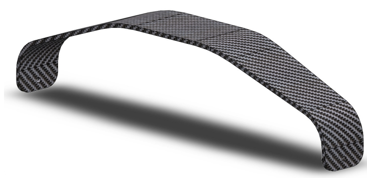

Figure 4.12: Final shape configuration of the landing gear in *SolidWorks*

4.4.2 FEM Analysis - Composite Lay-Up

In order to analyse the behaviour of different carbon fiber composite lay-ups, the team ran simulations in *Ansys Static Structural*. According to figure 4.13, it is noticeable that less bending deformation occurs when the landing gear is composed of uni-directional 0° carbon fibers, in relation to the other two lay-ups. In this study, the 0° fibers are aligned with the y axis of the airplane.

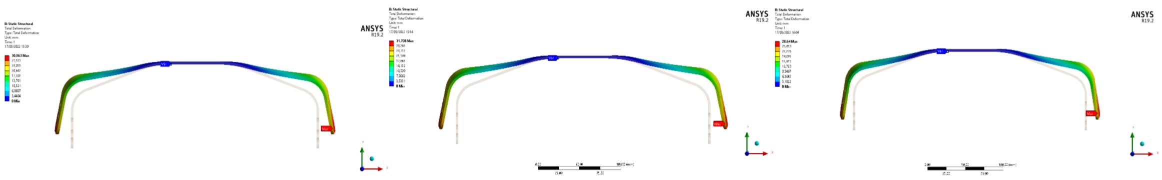

(a) 0_3/Airex-Core/0_3 **(b)** 0/45/0/Airex-Core/0/45/0 **(c)** 0/UD-0/0/Airex-Core/0/UD-0/0

Figure 4.13: Deformation for 3 different landing gear composite lay-ups with the same shape and simulating a two wheel landing in *Ansys Static Structural*

It was also simulated a one wheel landing to analyse the torsion capacity of different composite lay-ups, as shown in figure 4.14. Comparing the six layers of 0° placed fibers to only two layers at 0° combining with one 45° layer, the torsion deformation was almost the same. Therefore, it is better to incorporate a 45° placed fiber instead of three more 0° fibers, reducing unnecessary weight.

Finally, the combination of the studies aforementioned lead to an optimised composite lay-up that reduces bending and torsion deformation in various landing situations with the lay-up being: [0/UD-0/45/0/Airex Core/0/45/UD-0/0] and its FEM simulation is in fig. 4.15.

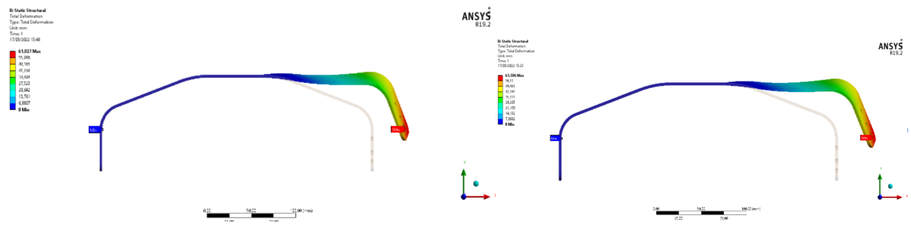

(a) 0_6/Airex Core/0_6 **(b)** 0/45/0/Airex Core/0/45/0

Figure 4.14: Deformation for 2 different landing gear composite lay-ups with the same shape and simulating an one wheel landing (in Ansys Static Structural)

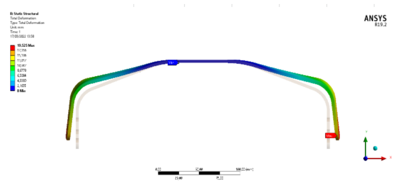

Figure 4.15: Deformation of landing gear with the final composite lay-up in a two wheel landing simulation (in *Ansys Static Structural*)

4.4.3 Wheels

Using the work of Cascini et al. [8] as reference for the front wheel design, the aerodynamics task-force established that a satisfactory wheel would be thin and of a relatively high diameter. Instead of purchasing a wheel with such parameters, the team designed and optimised their own 3D printed wheels, using PETG filament (figure 4.16). The outside perimeter of the wheels is covered with a hard foam material. The wheels have an outer diameter of 128 mm and a thickness of 12 mm.

To fulfill the taildragger configuration, the team choose to use a third wheel for the rear (as seen in figure 4.17), after field testing, with a significantly smaller size than the front wheels, as seen in aircraft with this landing gear configuration. The placement of the 25 mm diameter and 9 mm thick back wheel - purchased at a local hobby store - was contingent to the requirements set and, after some research, the team decided to use a hand-bent steel rod (with a 3 mm diameter) to meet this requirement, attached to the tailboom via two 3D printed pieces that allow the fastening of the screws in the stabilizers. The use of this rod also allows for fine tuning of the aircraft's angle of attack before take-off.

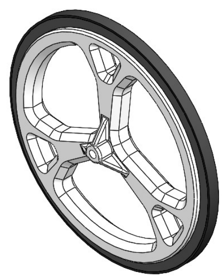

Figure 4.16: Landing gear front wheel in SolidWorks

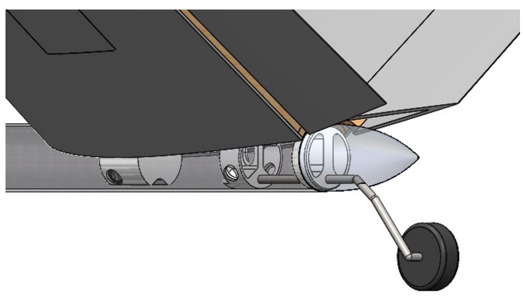

Figure 4.17: Landing gear rear wheel in *SolidWorks*

5 Manufacturing of the UAV Components

All the components of the UAV were manufactured using similar methods. The wing, fuselage and stabilizers are made from composite shells, which require the production of external molds. For the wings and fuselage, medium-density fiberboard (MDF) sheets were machined by the team using CNC software and then treated with epoxy resin. For the stabilizers, the moulds were obtained by additive manufacturing (fused deposition modelling of PETG filament). All composite manufacturing resorted to hand lay-up and vacuum bagging techniques.

The assembly of the internal structure of the wing and stabilizers resorted to alignment pieces, as seen in 5.1b, which ensures the alignment of connections and the correct angles of attack. All the internal structures were fixed using epoxy resin mixed with lightweight glass microspheres, which reduce the overall density.

The wing spars were made by winding the impregnated carbon fiber to the balsa sheets cut previously. The wing connection tubes were manufactured with a similar procedure, but removing the wood inside the fiber after the CFRP has been cured.

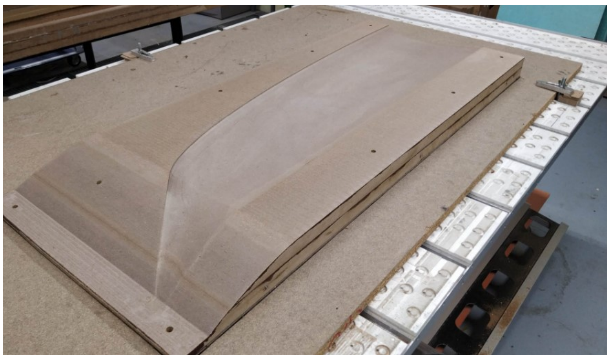

(a) Mold

(b) Internal structure

Figure 5.1: Construction of the wing

(a) Mold

(b) Internal structure

Figure 5.2: Construction of the fuselage

(a) Mold **(b)** Assembly of the servo linkages

Figure 5.3: Construction of the stabilizers

(a) Composite manufacturing **(b)** 3D printing of the front wheels

Figure 5.4: Construction of the landing gear and wheels

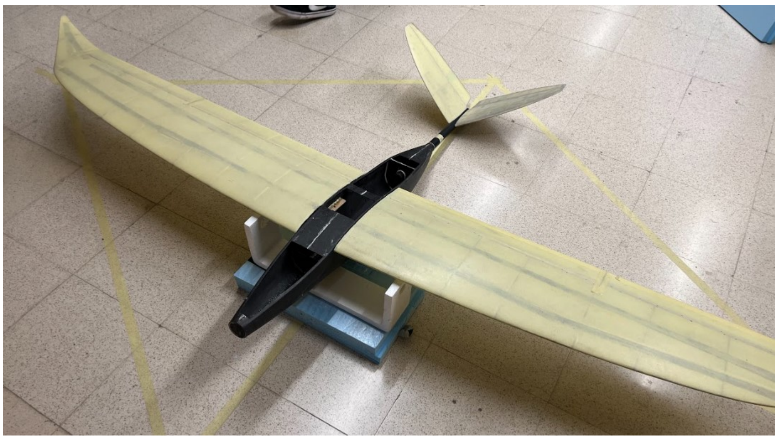

Figure 5.5: Assembly of the UAV

6 Outlook

These past two years were marked by a significant improvement in the methods that the team used to design and build an unmanned aerial vehicle, all the way from the programs developed to address specific requirements of the competition and determine optimal design solutions, to the manufacturing methods learned which permitted building complex geometries with repeatability. All the knowledge acquired and challenges overcame led the team closer to the presented UAV in this technical report, which is believed to be the most intricate and developed design the team has ever created.

The team is optimistic about the groundwork of design and manufacturing designs that these processes have laid out for the future, allowing fast prototyping, adaptability and creating more resources to develop other challenging UAV configurations.

The internal schedule compliance, within a small margin, is noteworthy: for the first time in the last ACC editions, the Olissipo Air Team managed to build the UAV two months ahead of the competition date. That means there is time to improve flaws in the design and rebuild whichever parts prove to be the worst-performing, after some flight tests.

Nevertheless, there's still work to be carried throughout this time in evaluating the performance of the UAV, identifying flaws and correcting them, defining a flight plan for the competition and preparing the video presentation.

References

[1] Snorri Gudmundsson. *General Aviation Aircraft Design*. Elsevier, 2014.
[2] *hikersbay*. `http://hikersbay.com/climate/july/germany/munich?lang=en`. Accessed: 2022-04-27.
[3] *World Weather*. `https://world-weather.info/forecast/germany/munich/july-2021/`. Accessed: 2022-04-27.
[4] João Oliveira. "Apontamentos de Estabilidade de Voo". In: (2019), pp. 207–209.
[5] J.E. Smithn A.E. Eiben. *Introduction to Evolutionary Computing*. Springer, 2003.
[6] T. H. G. Megson. *Aircraft Structures for engineering students*. Elsevier, 2007.
[7] Christos Kassapoglou. *Design and Analysis of Composite Structures*. Wiley, 2013.
[8] Cascini. "Computer-Aided Conceptual Design Through TRIZ-based Manipulation of Topological Optimizations". In: (2009).

Annex

A Drawings

Table A.1: Drawings

Drawing Number	**Drawing Description**
OAT - 1	3-View Drawing
OAT - 2	Isometric View Drawing
OAT - 3	Cargo-Bay 3-View Drawing
OAT - 4	Exploded View Drawing

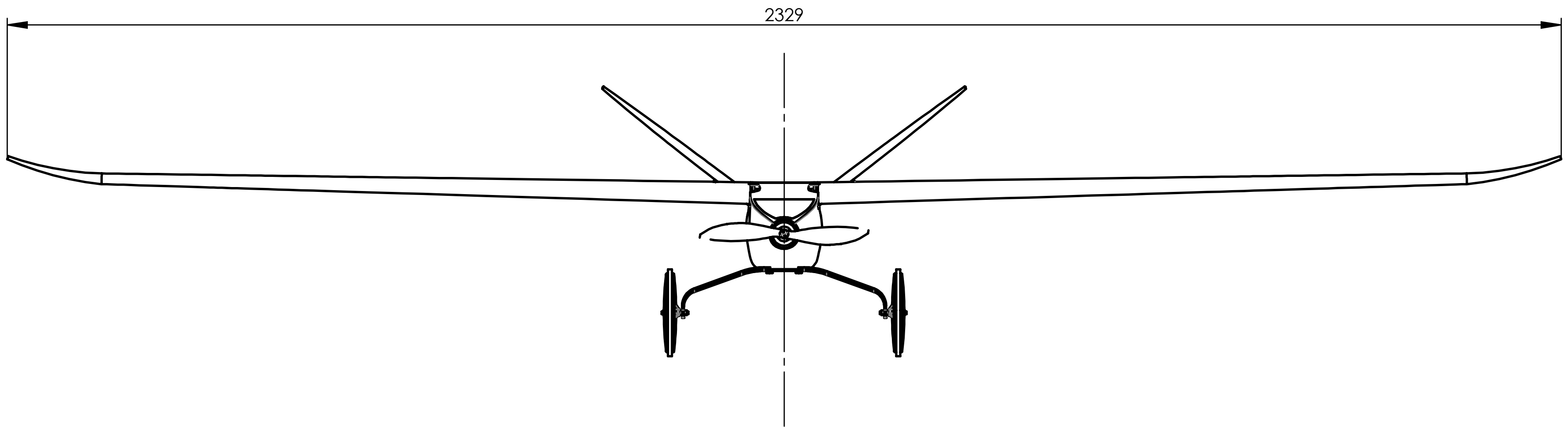

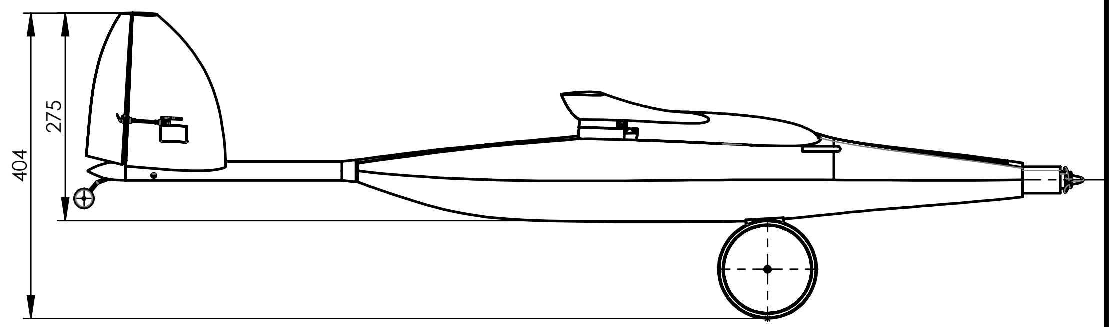

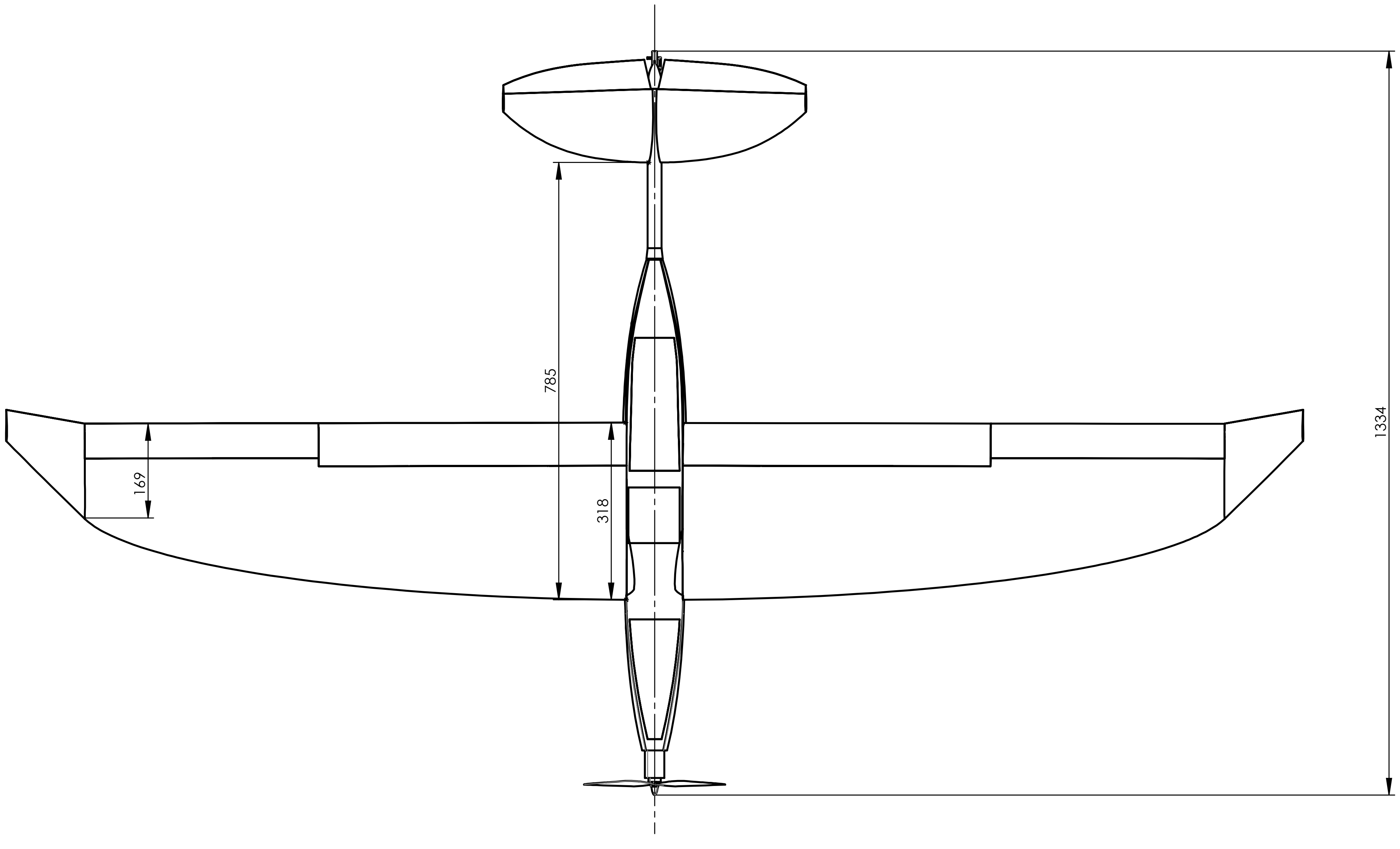

Aircraft relevant data		
Airfoil profile	Wing	Designed by us*
	Tail	NACA 0008
Area (mm^2)	Wing	680 000
	Tail	100 000
Span (mm)	Wing	2329
	Tail	680
Aspect ratio	Wing	7.98
	Tail	4.66
Wing chord (mm)	root	318
	tip	169
Tail chord (mm)	root	185
	tip	46
Dihedral angle (°)	Wing	1.5
	Tail	37
Stationary angle of attack (°)		9.15
Angle of attack (°)	Wing	0
	Tail	2.5
Volume (mm^3)	Cargo bay	7 515 000
	Cargo Space	5 394 000
CG estimated position (mm from the leading edge)		118

Scale: 1:10

Material:

Notes:
* This airfoil was created by us, from scratch, the process is explained in detail in the tecnical report

Olissipo Air team
Team 6

TÉCNICO LISBOA

Aircraft: 3-view drawing

Sheet	Component Code	Page	Mass:	Author
A3	OAT	1	2180g	João Gaspar

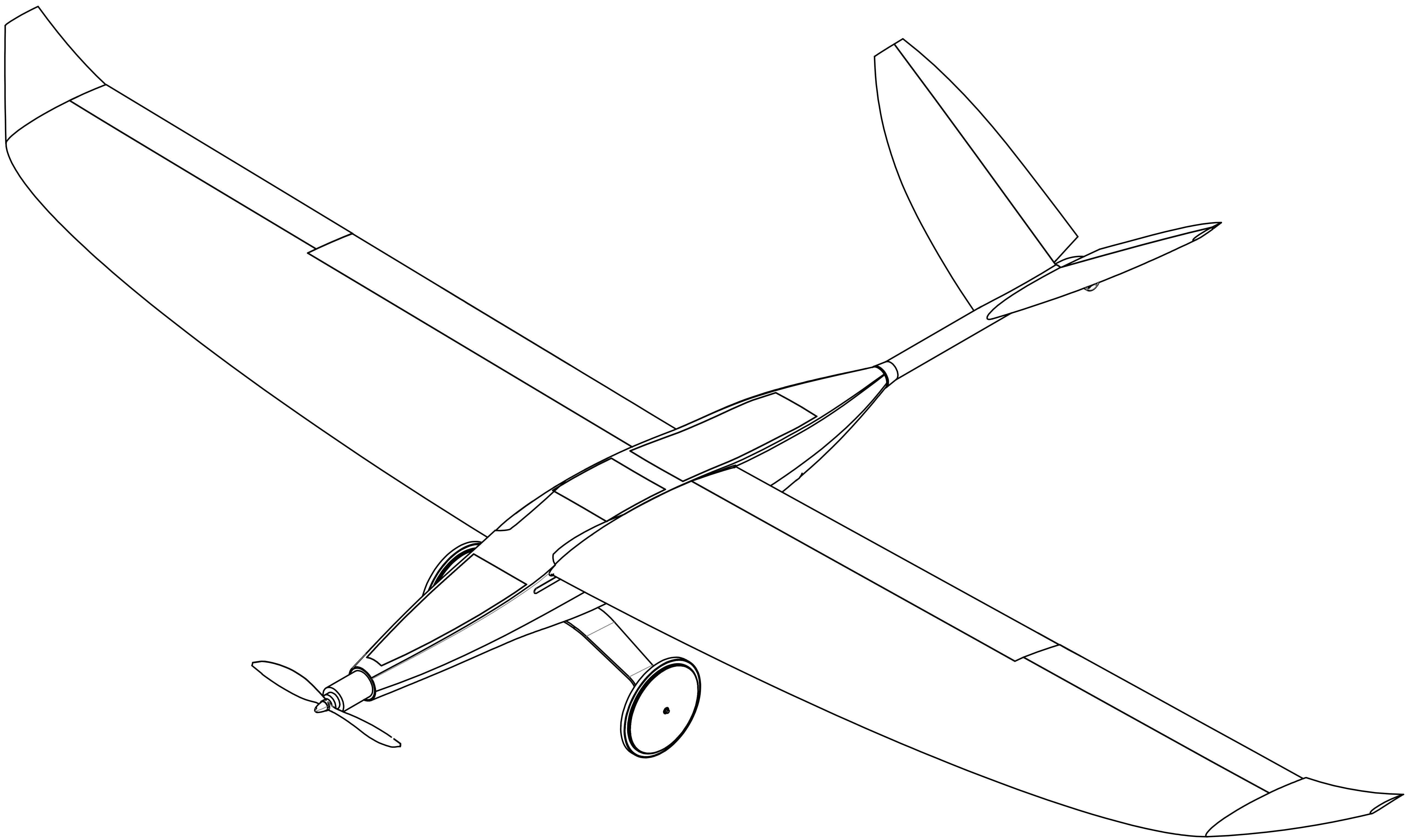

Scale: 1:5	Olissipo Air team	
Material:	Team 6	TÉCNICO LISBOA
Notes:	Aircraft: Isometric view	

Sheet	Component code	Page	Mass:	Author
A3	OAT	2	2180g	João Gaspar

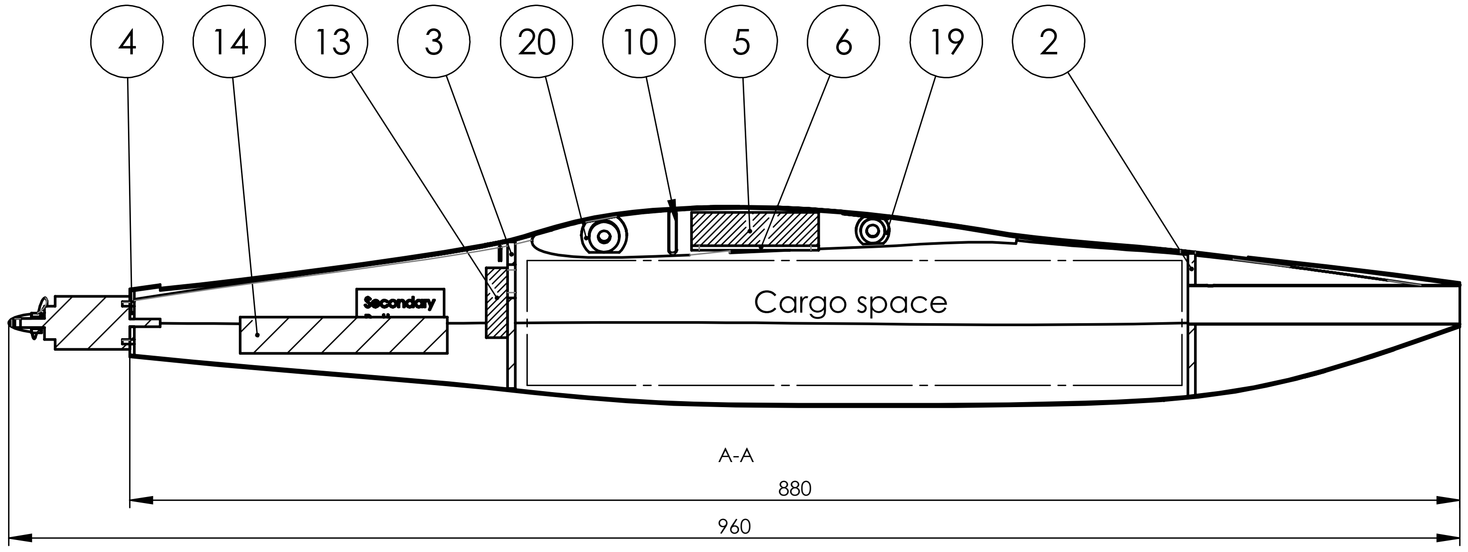

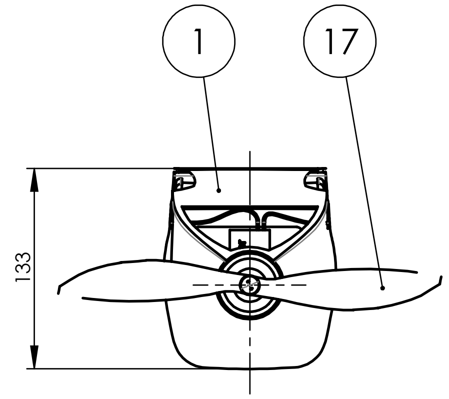

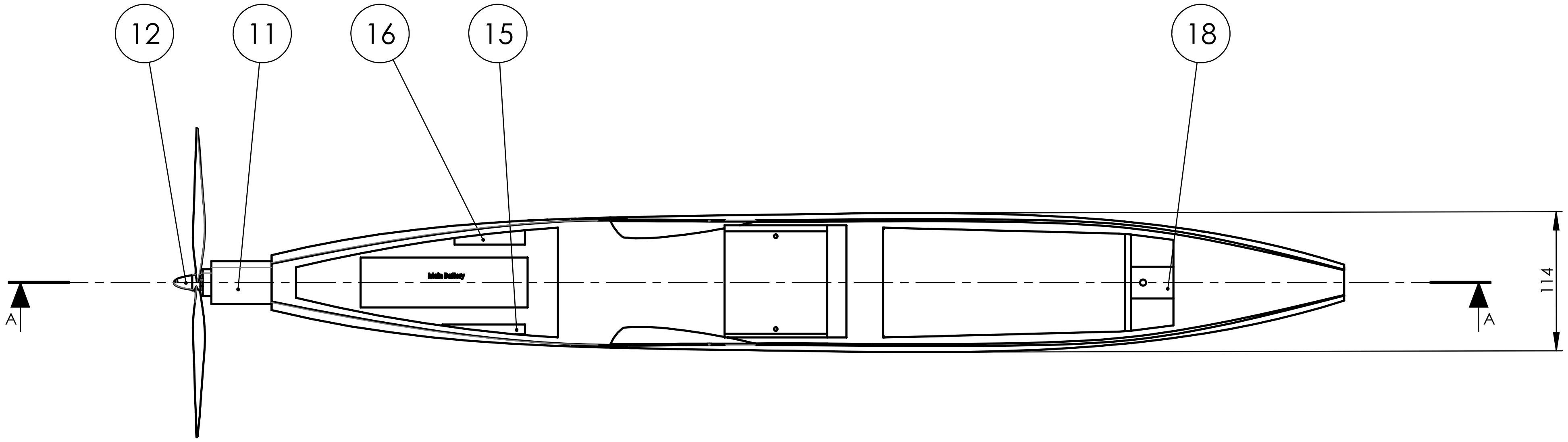

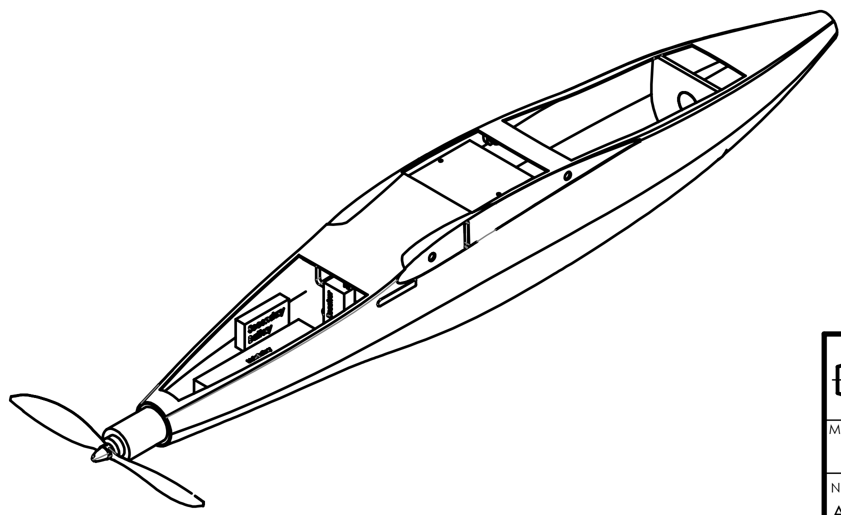

Nº	Name	Qty	Obs.
1	CargoBay_Structure	1	
2	Tail_Support	1	
3	Eletro_Support	1	
4	Motor_Support	1	
5	GPS _System	1	
6	GPS_Support	2	
7	GPS_Lid	1	
8	Eletro_Lid	1	
9	Bags/Cargo_Lid	1	
10	Wing_sleeve	1	
11	Motor	1	
12	Spinner	1	
13	Receiver_X8R and Antennas	1	
14	main_battery	1	
15	esc	1	
16	secondary_battery	1	
17	Propeller	1	
18	Tail boom fitting	1	
19	Spar fitting_ Back	2	
20	Spar fitting	2	

Scale: 1:5

Material:

Notes:
All three lids have been removed, in order to see what is inside

Olissipo Air team
Team 6

TÉCNICO LISBOA

Cargo Bay: 3-view drawing

Sheet	Component code	Page	Mass:	Author
A3	OAT_CB	3	1025g	João Gaspar

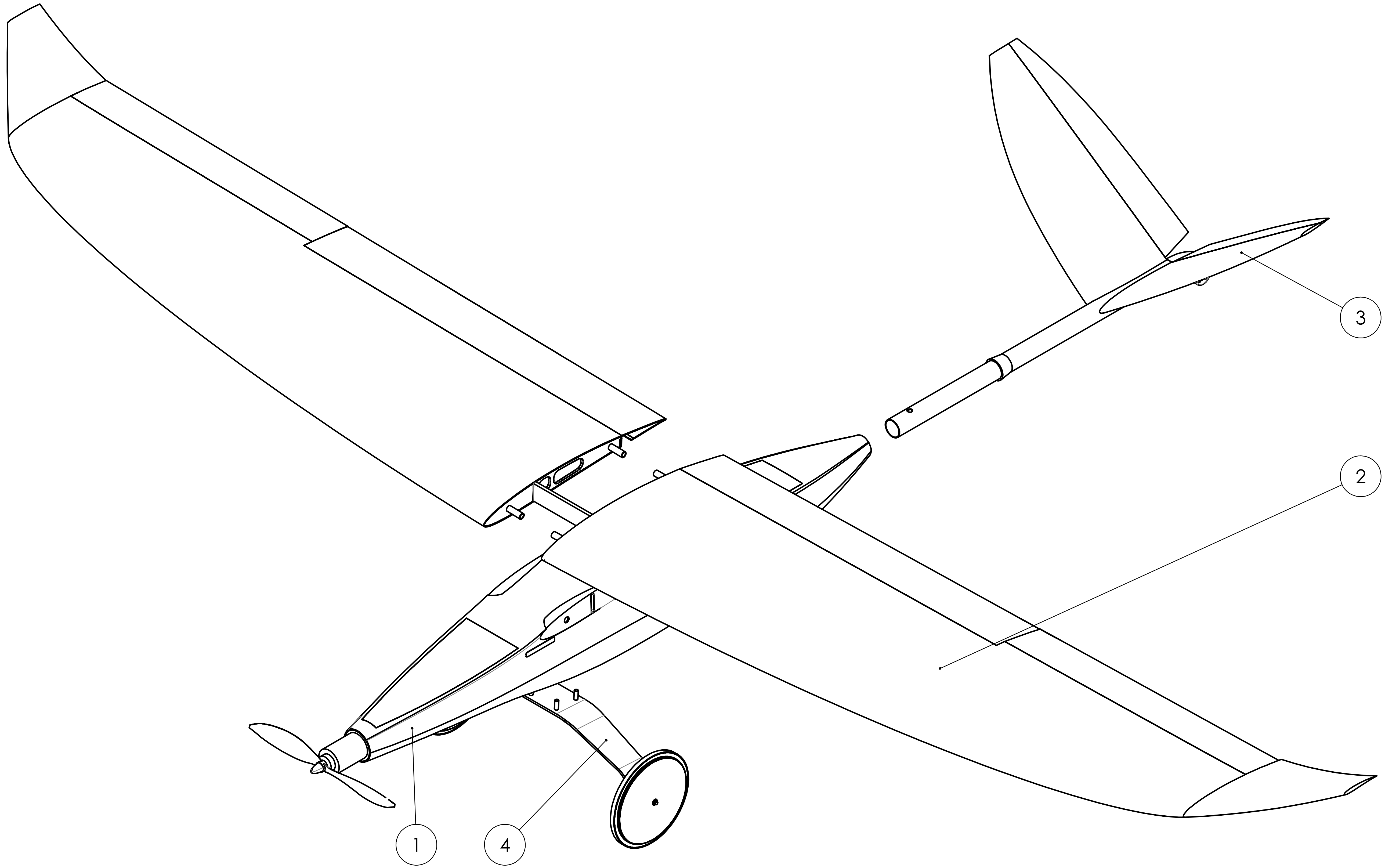

Nº	Name	Qty	Component code	Mass (g) *	Obs.
1	Cargo Bay	1	OAT_Olissipo_CB	1025	
2	Wing	1	OAT_Olissipo_W	770	
3	Tail + Tail boom	1	OAT_Olissipo_T	235	
4	Landing Gear	1	OAT_Olissipo_LG	150	

Scale: 1:5

Material:

Notes:
* The mass of each part was measured from our first physical prototype

Olissipo Air team
Team 6

TÉCNICO LISBOA

Aircraft: Exploded view

Sheet	Component code	Page	Mass:	Author
A3	OAT	4	2180g	João Gaspar

B Team Members

Table B.1: Team Members - Olissipo Air Team 2022.

Name	Team position	Course
Afonso Rodrigues Lourenço	Tail and landing gear Team Member	Aerospace Eng.
André Calado Marta	Supervising Professor	-
Beatriz Gonçalves Contente	Fuselage Team Member	Aerospace Eng.
Berke Duarte dos Santos	Marketing Team Member	Aerospace Eng.
Carlos Miguel Ferreira Ribeiro	Tail and landing gear Team Member	Aerospace Eng.
Catarina João Fonseca Santos	Wing structures Team Member	Aerospace Eng.
Diogo Luis Miragaia Soares Bravo	Wing structures Team Member	Aerospace Eng.
Duarte Miguel Mestre de Brito	Financial management Coordinator / Aerodynamics Coordinator	Aerospace Eng.
Eryk Swolkien Sousa	Wing structures Team Member	Aerospace Eng.
Eva Rodrigues Dias Claro	Wing structures Team Member	Aerospace Eng.
Filipe Calderon de Cerqueira Rocha e Faria	Tail and landing gear Coordinator	Aerospace Eng.
Francisco António Domingos Alves	Wing structures Team Member	Aerospace Eng.
Francisco de Jesus Jorge Dores	Fuselage Coordinator	Aerospace Eng.
Francisco da Silva Parreira de Castro Fonseca	Electronics Team Member	Aerospace Eng.
Francisco Manuel Carneiro Pinto Branco Carvalho	Aerodynamics Team Member	Aerospace Eng.
Gonçalo Manuel Neves Coelho	Aerodynamics Team Member	Aerospace Eng.
Guilherme Fernandes Lourenço	Aerodynamics Team Member	Aerospace Eng.
Henrique Duarte Hachmeister Caraça	Aerodynamics Team Member	Aerospace Eng.
Henry Machado Vilas Boas	Wing structures Team Member	Aerospace Eng.
Hugo Tavares Freire	Aerodynamics Team Member	Mechanical Eng.
Joana Margarida Carreiro Santana	Tail and landing gear Team Member	Aerospace Eng.
João Ferreirinha Guimarães dos Santos	Fuselage Team Member	Aerospace Eng.
João Miguel Gomes Gaspar	Tail and landing gear Team Member	Aerospace Eng.
João Pedro Almeida Machado	Wing structures Team Member	Aerospace Eng.
João Tomás Ferreira Diniz	Wing structures Team Member	Aerospace Eng.
José Luís Pereira Coelho	Fuselage Team Member	Aerospace Eng.
José Miguel Bento	Human Resources Coordinator / Electronics Coordinator	Aerospace Eng.
José Miguel Luzia Murteira	Fuselage Team Member	Aerospace Eng.
Letícia Carvalho Pereira de Araújo	Fuselage Team Member	Aerospace Eng.
Ludovico Lourenço	Pilot	-
Manuel Maria Sanina do Espírito Santo e Silva	Marketing Team Member	Mechanical Eng.
Maria Cabral de Meireles e Magalhães	Aerodynamics Team Member	Aerospace Eng.
Maria José Quitério de Oliveira Redondo	Marketing Team Member	Aerospace Eng.
Mariana Fernandes Gago	Marketing Team Member	Mechanical Eng.
Mariana Pires Gonçalves Toco Dias	Marketing Coordinator	Mechanical Eng.
Max Brazhnyy	Aerodynamics Team Member	Mechanical Eng.
Miguel Barros Marques	Aerodynamics Team Member	Aerospace Eng.
Miguel Loureiro de Jesus	Fuselage Team Member	Aerospace Eng.
Nuno Miguel Calvo Matos	Aerodynamics Team Member	Aerospace Eng.
Nuno Manuel Almeida Ribeiro	Fuselage Team Member	Aerospace Eng.
Pedro Guilherme de Almeida Borges	Aerodynamics Team Member	Aerospace Eng.
Pedro Miguel Gonçalves da Silva Timóteo	Wing structures Team Member	Aerospace Eng.
Raquel Roxo Couto	Tail and landing gear Team Member	Aerospace Eng.
Rúben Miguel Duarte Novais	Aerodynamics Team Member	Aerospace Eng.
Simão Machado Martins	Team Leader / Wing structures Coordinator	Aerospace Eng.
Tiago João Fachadas Escalda	Electronics Team Member	Aerospace Eng.
Tomás Trindade Nunes	Electronics Team Member	Aerospace Eng.
Vasco Manuel Domingues Cotão	Aerodynamics Team Member	Aerospace Eng.

C Forces and Moments Applied in the Aircraft

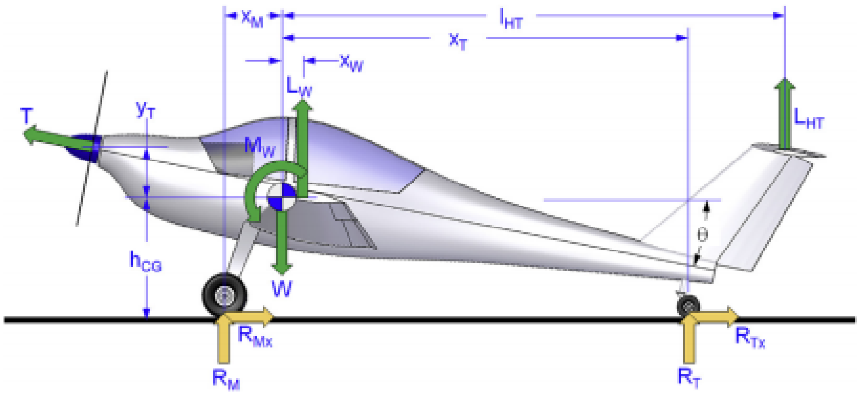

Figure C.1: Forces and moments applied in the aircraft [1]

D Airfoil Data

Table D.1: Data Sheet of tip airfoil

x	y	x	y
0.99997	-0.00478	0.00005	0.00190
0.99474	-0.00244	0.00000	0.00000
0.98542	-0.00026	0.00020	-0.00190
0.97404	0.00192	0.00069	-0.00378
0.96057	0.00434	0.00148	-0.00566
0.94523	0.00700	0.00257	-0.00754
0.92861	0.00987	0.00397	-0.00936
0.91130	0.01283	0.00567	-0.01114
0.89369	0.01583	0.00768	-0.01288
0.87597	0.01886	0.00999	-0.01457
0.85824	0.02186	0.01268	-0.01623
0.84053	0.02483	0.01576	-0.01788
0.82290	0.02776	0.01929	-0.01951
0.80531	0.03063	0.02338	-0.02114
0.78767	0.03346	0.02810	-0.02277
0.77013	0.03628	0.03364	-0.02441
0.75276	0.03900	0.04014	-0.02605
0.73537	0.04162	0.04778	-0.02767
0.71799	0.04416	0.05678	-0.02924
0.70063	0.04662	0.06722	-0.03072
0.68328	0.04897	0.07911	-0.03203
0.66594	0.05123	0.09232	-0.03314
0.64858	0.05340	0.10662	-0.03399
0.63125	0.05547	0.12174	-0.03458
0.61390	0.05743	0.13748	-0.03493
0.59657	0.05930	0.15369	-0.03505
0.57923	0.06107	0.17025	-0.03495
0.56190	0.06272	0.18708	-0.03468
0.54456	0.06427	0.20412	-0.03424
0.52722	0.06571	0.22133	-0.03367
0.50989	0.06706	0.23869	-0.03298
0.49257	0.06828	0.25617	-0.03219
0.47525	0.06940	0.27375	-0.03130
0.45794	0.07040	0.29143	-0.03035
0.44066	0.07129	0.30919	-0.02932
0.42340	0.07205	0.32701	-0.02825
0.40616	0.07269	0.34490	-0.02714
0.38895	0.07319	0.36286	-0.02598
0.37178	0.07358	0.38087	-0.02482
0.35464	0.07382	0.39892	-0.02362
0.33755	0.07391	0.41700	-0.02244
0.32051	0.07386	0.43506	-0.02125
0.30354	0.07365	0.45308	-0.02007
0.28664	0.07329	0.47106	-0.01892
0.26981	0.07276	0.48901	-0.01779
0.25308	0.07204	0.50692	-0.01670
0.23645	0.07114	0.52479	-0.01564
0.21994	0.07004	0.54264	-0.01462
0.20359	0.06874	0.56045	-0.01366
0.18740	0.06722	0.57824	-0.01274
0.17141	0.06548	0.59600	-0.01188
0.15569	0.06350	0.61374	-0.01107
0.14026	0.06126	0.63148	-0.01032
0.12522	0.05877	0.64920	-0.00965
0.11067	0.05603	0.66692	-0.00902
0.09674	0.05305	0.68463	-0.00846
0.08361	0.04986	0.70233	-0.00797
0.07148	0.04653	0.72005	-0.00754
0.06053	0.04314	0.73777	-0.00717
0.05087	0.03977	0.75552	-0.00687
0.04253	0.03652	0.77328	-0.00662
0.03541	0.03340	0.79107	-0.00644
0.02939	0.03048	0.80887	-0.00630
0.02428	0.02773	0.82671	-0.00621
0.01993	0.02514	0.84458	-0.00617
0.01623	0.02268	0.86248	-0.00617
0.01305	0.02034	0.88040	-0.00620
0.01032	0.01809	0.89832	-0.00626
0.00800	0.01593	0.91618	-0.00634
0.00600	0.01382	0.93385	-0.00644
0.00431	0.01175	0.95101	-0.00654
0.00291	0.00970	0.96710	-0.00663
0.00180	0.00770	0.98137	-0.00671
0.00095	0.00574	0.99331	-0.00676
0.00037	0.00381	0.99997	-0.00678

Table D.2: Data Sheet of root airfoil

x	y	x	y
1.00000	0.00847	0.00025	0.00046
0.99899	0.00962	0.00226	-0.00371
0.99598	0.01092	0.00628	-0.00765
0.99096	0.01240	0.01229	-0.01131
0.98397	0.01407	0.02025	-0.01465
0.97504	0.01597	0.03015	-0.01764
0.96418	0.01809	0.04195	-0.02025
0.95146	0.02045	0.05558	-0.02246
0.93693	0.02307	0.07101	-0.02424
0.92063	0.02593	0.08816	-0.02561
0.90263	0.02903	0.10697	-0.02655
0.88302	0.03235	0.12737	-0.02710
0.86187	0.03587	0.14926	-0.02727
0.83925	0.03953	0.17257	-0.02709
0.81528	0.04330	0.19720	-0.02661
0.79003	0.04711	0.22304	-0.02586
0.76361	0.05102	0.25000	-0.02490
0.73614	0.05483	0.27797	-0.02375
0.70771	0.05849	0.30683	-0.02245
0.67844	0.06196	0.33647	-0.02105
0.64846	0.06517	0.36676	-0.01958
0.61788	0.06808	0.39760	-0.01805
0.58682	0.07066	0.42884	-0.01650
0.55542	0.07287	0.46037	-0.01494
0.52379	0.07468	0.49207	-0.01339
0.49207	0.07606	0.52379	-0.01187
0.46037	0.07701	0.55542	-0.01038
0.42884	0.07750	0.58682	-0.00894
0.39760	0.07753	0.61788	-0.00754
0.36676	0.07709	0.64846	-0.00621
0.33647	0.07619	0.67844	-0.00494
0.30683	0.07484	0.70771	-0.00374
0.27797	0.07306	0.73614	-0.00262
0.25000	0.07087	0.76361	-0.00159
0.22304	0.06829	0.79003	-0.00066
0.19720	0.06535	0.81528	0.00018
0.17257	0.06209	0.83925	0.00091
0.14926	0.05854	0.86187	0.00154
0.12737	0.05473	0.88302	0.00207
0.10697	0.05069	0.90263	0.00250
0.08816	0.04645	0.92063	0.00284
0.07101	0.04204	0.93693	0.00310
0.05558	0.03751	0.95146	0.00327
0.04195	0.03287	0.96418	0.00337
0.03015	0.02816	0.97504	0.00342
0.02025	0.02342	0.98397	0.00342
0.01229	0.01868	0.99096	0.00338
0.00628	0.01397	0.99598	0.00332
0.00226	0.00934	0.99899	0.00323
0.00025	0.00482	1.00000	0.00312

E FEM Analysis Parameters

Table E.1: Isotropic Materials' Properties

Isotropic Materials	Balsa Wood	Airex Core
Young's Modulus $[GPa]$	2.55	0.35
Poisson's Ratio	0.38	0.3
Tensile Strength $[MPa]$	73	-

Table E.2: Composite Materials' Properties

Composite	Std Carbon Fabric	E-Glass fabric
$E_1[MPa]$	63000	25000
$E_2[MPa]$	63000	25000
ν_{12}	0.06	0.17
$G_{12}[MPa]$	3500	4410
$G_{13}[MPa]$	3500	4410
$G_{23}[MPa]$	3500	4410
$X_t[MPa]$	600	440
$X_c[MPa]$	570	300
$Y_t[MPa]$	600	440
$Y_c[MPa]$	570	300
$S[MPa]$	90	40

Table E.3: Minimum Margin of Safety obtained for the optimized wing structures.

Wing Structure	$MoS(climb)$	K (factor of safety)
Shell (composite)	0.04	1.58
Spar (composite)	0.45	1.58
Spar (balsa, isotropic)	4.18	1.58

F Wing Internal Structure - Final Results

Table F.1: Final design of the spar with 4 sections, after FEM optimisation

Spar Section	Beginning	End	CFRP layers	UD reinforcement	Pos. in chord
1 (Conn. Tube)	0cm	30cm	2	-	28%
1 (Central Spar)	0cm	30cm	3	3	28%
2	30cm	50cm	1	3	28%
3	50cm	97cm	0	3	20%
4 (Winglet)	97cm	107cm	0	2	28%

Table F.2: Panels between ribs and estimated deflection (in climb)

Panels	Beginning (cm)	End (cm)	Max. Deflection (mm)
1	0	13.9	0.33
2	13.9	26.5	0.32
3	26.5	38.2	0.37
4	38.2	55	0.28
5	55	67	0.33
6	67	82.5	0.24
7	82.5	96.9	0.24
8	96.9	107	0.09